

Review

Recent Advances in Photo–Activated Chemical Sensors

Dong Hyun Lee and Hocheon Yoo * 

Department of Electronic Engineering, Gachon University, 1342 Seongnam–daero,
Seongnam 13120, Republic of Korea

* Correspondence: hyoo@gachon.ac.kr

Abstract: Gas detectors have attracted considerable attention for monitoring harmful gases and air pollution because of industry development and the ongoing interest in human health. On the other hand, conventional high–temperature gas detectors are unsuitable for safely detecting harmful gases at high activation temperatures. Photo–activated gas detectors improve gas sensing performance at room temperature and enable low–power operation. This review presents a timely overview of photo–activated gas detectors that use illuminated light instead of thermal energy. Illuminated light assists in gas detection and is classified as visible or ultraviolet light. The research on photo–activated gas detectors is organized according to the type of gas that can be intensively detected. In addition, a development strategy for advancing photo–activated gas detectors is discussed.

Keywords: photo–activated gas detectors; ultraviolet; visible light; nitric oxide; nitric dioxide; formaldehyde; ammonia



Citation: Lee, D.H.; Yoo, H. Recent Advances in Photo–Activated Chemical Sensors. *Sensors* **2022**, *22*, 9228. <https://doi.org/10.3390/s22239228>

Academic Editor: Antonio Di Bartolomeo

Received: 1 November 2022

Accepted: 23 November 2022

Published: 27 November 2022

Publisher’s Note: MDPI stays neutral with regard to jurisdictional claims in published maps and institutional affiliations.



Copyright: © 2022 by the authors. Licensee MDPI, Basel, Switzerland. This article is an open access article distributed under the terms and conditions of the Creative Commons Attribution (CC BY) license (<https://creativecommons.org/licenses/by/4.0/>).

1. Introduction

Gas detectors have attracted enormous attention because they can detect the emergence of a gas in areas of development for particular safety systems. To be specific, gas detectors offer rapid detection for early response to tremendous accidents with flammable [1–9], combustible gases [10–15], as well as bio–hazardous gases [16–25]. These devices are widely used in industry for continuously monitoring gas leakages [26–29] or manufacturing processes [30–33]. Gas detectors can be classified according to their operation principles: electrochemical devices [34–37], photoionization–based types [38–41], ultrasonic detectors [42–45], and semiconductor–based devices [46–49]. Among the various detector types, semiconductor–based devices allow rapid gas detection because the electrical resistance changes when it comes into contact with the target gas. Semiconductor–based gas detectors have been developed, and a variety of detectors have been reported using semiconducting materials, such as metal oxides [50–54], carbon nanotubes [55–58], two–dimensional materials, including graphene [59–62] and transition metal dichalcogenide [63–66], organic materials [67–70], and perovskites [71–74]. On the other hand, these detectors suffer cross–sensitivity with other gases; high reactivity with gases other than the target gas reduces selectivity [75–77]. Furthermore, the demand for faster recovery rates [78–80] and improved responsiveness in detecting extremely small amounts of gas [81–84] is driving the continuous development of these detectors. As an emerging approach, photo–activated or photo–assisted gas detection over diverse materials and devices has been proposed. By irradiating with light of a specific wavelength during the gas detection operation, this approach (1) enhances the photoreaction speed and recovery speed, (2) secures gas selectivity, and (3) increases the gas reactivity. The mechanism of gas sensors is different for each sensor device. Electron–hole pairs are generated by the interaction between the light irradiated on the photo–activated gas sensor and the surface of the gas–sensitive material. Photo–generated charge carriers interact with the oxygen ions of the gas–sensitive material, resulting in a change in conductivity. Figure 1 shows the surface statement of

an n-type metal oxide semiconductor-based photo-activated gas sensor by injecting oxidizing gas and reducing gas.

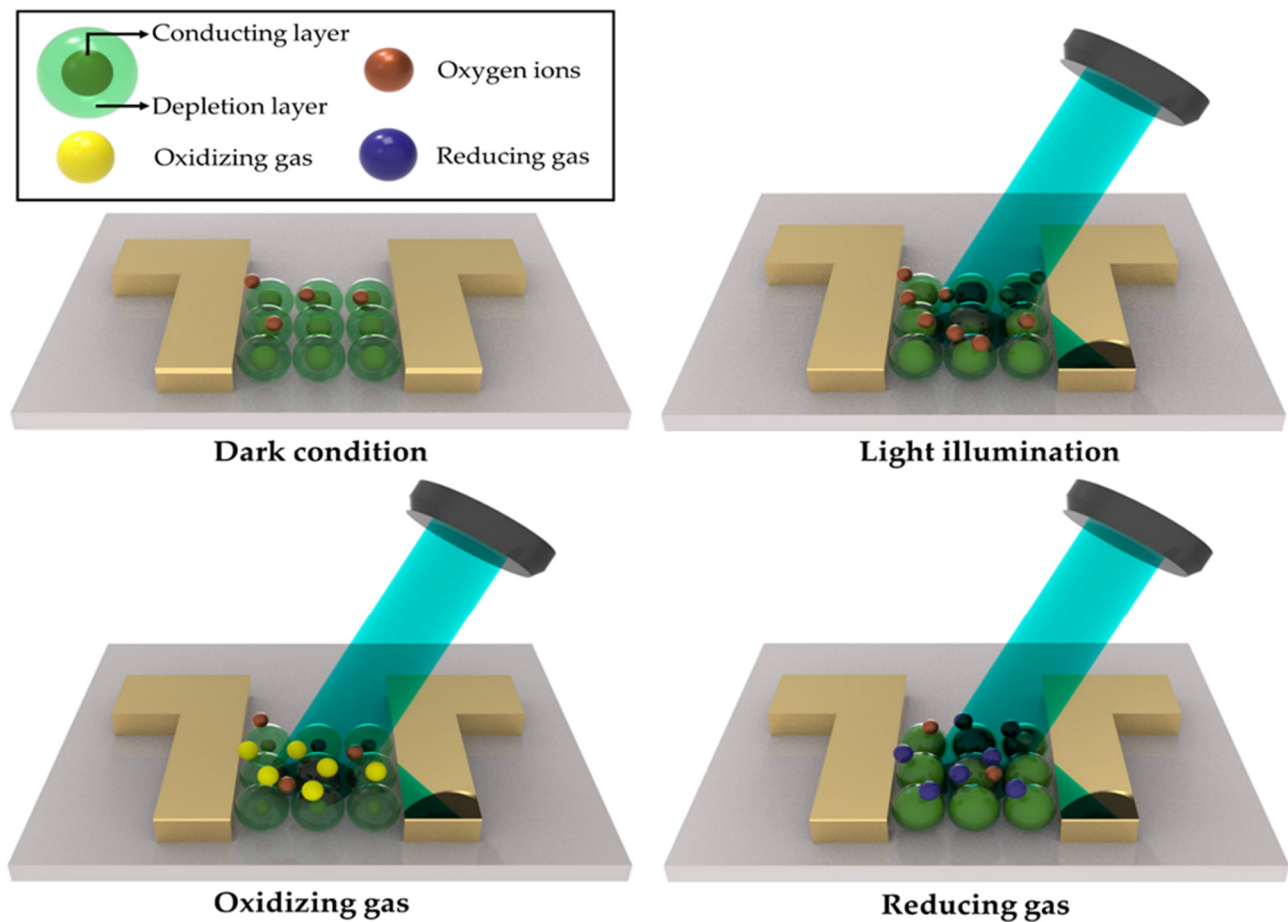


Figure 1. Surface state of n-type metal oxide semiconductor-based photo-activated gas sensor under oxidizing gas and reducing gas.

In this context, this review comprehensively revisits recent advances in photo-activated or photo-assisted gas detectors, emphasizing their illuminated light wavelengths and target gases. This paper reviews the recent developments in photo-activated gas detectors, classified according to the type of light source and target gas. The light sources for photo-activated gas detectors discussed in this review are ultraviolet and visible light. In addition, studies of photo-activated gas detectors with high selectivity for nitric oxide, nitric dioxide, formaldehyde, and ammonia gases are summarized. Finally, technology development strategies for photo-activated gas detectors are offered.

2. UV-Activated Gas Sensors

2.1. UV-Activated Nitric Oxide Gas Sensors

As a remarkable example of UV-activated nitric oxide gas detection, in 2020, Murali et al. presented NO gas detection using a heterojunction structure based on nitrogen-doped graphene quantum dots/titanium dioxide (TiO_2) named NGQDs [85]. The {001} facet form with unsaturated coordination atoms and dangling bonds led to more adsorbed oxygen-related gases on the TiO_2 surface, inducing high responsivity on the gas sensor platform. NGQDs were fabricated by doping graphene quantum dots (GQDs) with nitrogen atoms, which increased the gas-detecting performance of the heterostructure TiO_2 gas sensor by increasing the charge carriers and defects. Figure 2a shows the NO gas sensing characteristics of the TiO_2 @NGQDs sensor irradiated with UV light ($\lambda = 365 \text{ nm}$). The

response to 10–100 ppm NO gas was investigated. A higher concentration of injected NO gas increased the resistance of the TiO₂@NGQDs sensor. The measured response time and recovery time were 235 and 285 s, respectively (Figure 2b); they were 63 s and 605 s faster than under dark conditions. When irradiated with UV light, the response speed was improved due to the more active absorption and desorption of oxygen species on the TiO₂ surface than under dark conditions. Furthermore, the selectivity of the TiO₂@NGQDs sensor was investigated (Figure 2c). The TiO₂@NGQDs detected 100 ppm of NO, H₂S, H₂, and CO at room temperature. On the other hand, the response to NO gas was up to seven times higher than other gases. When n-type TiO₂ and p-type NGQDs have heterostructures, the excess electrons of TiO₂ move to NGQDs due to the relatively low bandgap of TiO₂. The NO gas injected into the TiO₂@NGQDs sensor interacts with surface oxygen ions and electrons in TiO₂, which reduces the carrier concentration of TiO₂. On the other hand, when the TiO₂@NGQDs sensor is irradiated with UV light, it interacts with the generated photoelectrons and oxygen on the surface to produce oxygen ions. The additionally generated UV light-induced oxygen ion species interact with the larger number of electrons in TiO₂.

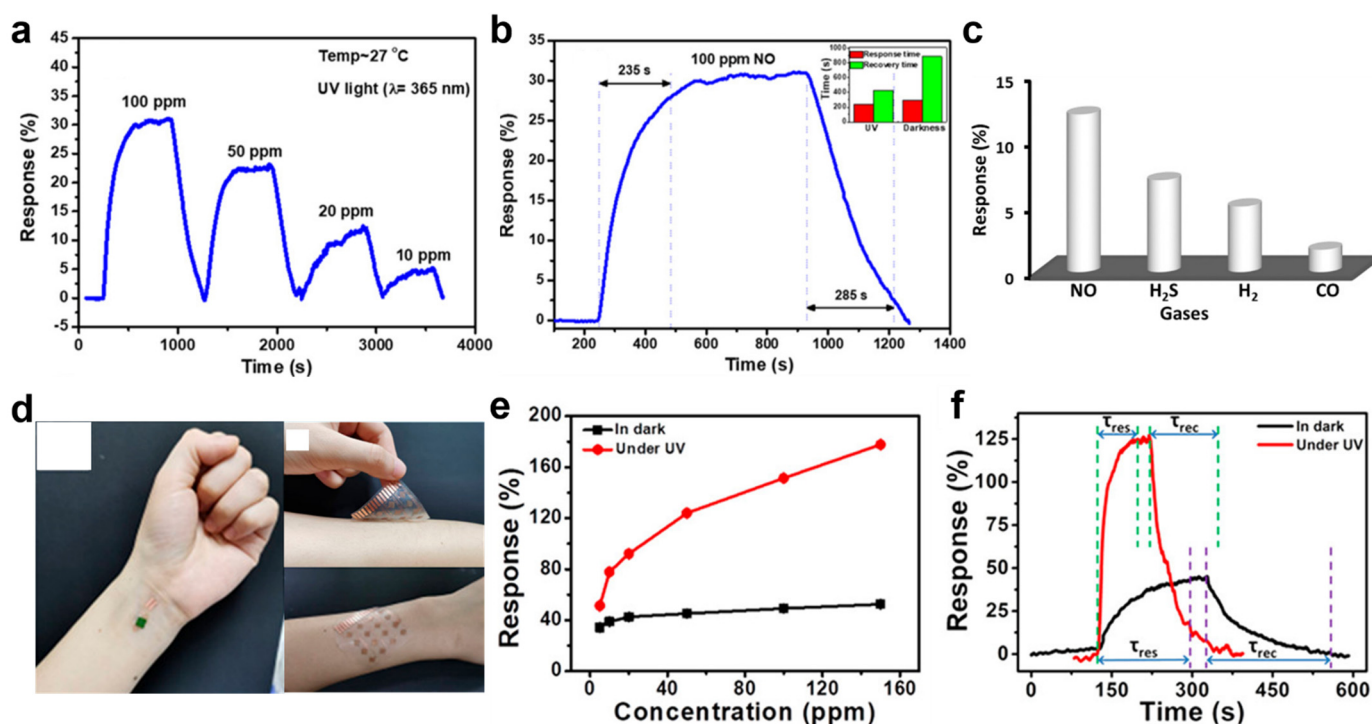


Figure 2. (a) Response of the TiO₂@NGQDs sensor under UV irradiated; (b) response and recovery times of TiO₂@NGQD sensors with UV-on and UV-off; (c) selectivity characteristics of the TiO₂@NGQDs sensor (adapted from [85] with permission from the American Chemical Society); (d) image of the flexible and wearable TiO₂@NGQDs sensor with human arm and wrist; (e) response of the Cu-TCA/TiNCs sensor ppb with UV-on and UV-off; (f) response and recovery time of the Cu-TCA/TiNCs sensor (adapted from [86] with permission from the American Chemical Society).

As another example, a p–n heterostructure was used to detect NO gas. He et al. represented a UV-activated NO gas sensor operable at room temperature using Cu-TCA (H3TCA = tricarboxytriphenylamine) and TiO₂ nanochannels (TiNCs) as a p–n heterostructure [86]. The Cu-TCA porous structure, due to the metal-organic framework (MOF), allows only the NO gas contained in the mixed gas to be adsorbed, providing selectivity for NO gas. In addition, the porous structure has many active sites for absorbing more NO molecules. The TiNCs as photocatalytic materials showed improved NO gas sensing characteristics owing to their high surface-to-volume ratio and stable chemical character-

istics. Figure 2d presents an image of a flexible Cu–TCA/TiNCs sensor attached to human skin. Polydimethylsiloxane (PDMS) was used as a substrate for the Cu–TCA/TiNCs sensor, and the S-shaped Cu electrode prevented damage due to fatigue deformation. The performance of the Cu–TCA/TiNCs sensor was improved when irradiated with UV light ($\lambda = 365$ nm). Figure 2e shows the NO gas response of the Cu–TCA/TiNCs sensor in dark and UV light-irradiated conditions with a range of 5–200 ppm NO gas injected. The NO gas response of the Cu–TCA/TiNCs sensor with UV light irradiation was increased from 1.5-fold to 3.4-fold compared with the dark condition. The UV irradiation effect reduced the response time of the Cu–TCA/TiNCs sensor owing to the large carrier concentration and active sites. Furthermore, the recovery time decreased owing to the accelerated activation of the surface to return to its initial state. Figure 2f shows the response speed of the Cu–TCA/TiNCs sensor. The response and recovery time were decreased by 101.2 s and 106 s compared to the dark conditions. The Cu–TCA/TiNCs sensor detected NO molecules due to a change in resistance by reactive oxygen species. The NO molecules capture electrons in the Cu–TCA/TiNC conduction band and interact with oxygen ions on the surface to form NO ions and N_2 ions. As a result, the NO and N_2 ions adsorbed on the surface increase the resistance of Cu–TCA/TiNC. On the other hand, UV light increases the response of the Cu–TCA/TiNCs sensor to NO gas. The electron-hole pairs generated by UV light produce many oxygen ions that interact more with the NO molecules in the dark. As a result, the width of the depletion layer was larger than in the dark, resulting in high resistance.

2.2. UV-Activated Nitric Dioxide Gas Sensors

As a representative UV-activated nitric dioxide gas detection study, in 2019, Wang et al. reported a nitric dioxide (NO_2) gas sensor with improved sensing performance by treating ZnO nanowires (NW) with $NaBH_4$ [87]. The oxygen vacancies (V_O) on the surface of the ZnO nanowires treated hydrothermally with $NaBH_4$ increase the chemisorption of oxygen species and NO_2 molecules. In addition, the UV irradiation effect generates many oxygen ions and promotes the formation of NO_3^- , which effectively improves the detection performance of NO_2 gas. Figure 3a,b show the changes in resistance of the ZnO nanowire sensor and the V_O -ZnO NW sensor with the $NaBH_4$ treatment. Under UV ($\lambda = 325$ nm) irradiation and dark conditions, the NO_2 gas sensors detected 1 ppm NO_2 gas. The variation in resistance of the NO_2 gas sensors depending on the initial air condition was 0.20 M Ω . Subsequently, when NO_2 gas was injected into the NO_2 gas sensors in the dark, the resistance of the V_O -ZnO NW was increased by approximately 2.25 M Ω compared to the ZnO NW. In other words, V_O -ZnO NW adsorbs many NO_2 molecules due to the increased surface defects, resulting in higher changes in resistance. Under UV irradiation, the NO_2 gas sensors showed resistance changes of 0.1 M Ω in air and 0.17 M Ω in NO_2 , respectively. UV irradiation enhanced the response and recovery time of the V_O -ZnO NW sensor. The response and recovery times of the V_O -ZnO NW sensor in UV irradiation conditions were 31 s and 144 s, respectively. The response and recovery times were reduced by 30 s compared to the dark conditions. Figure 3c shows the various gas sensing performances of the V_O -ZnO NW sensor under UV irradiation conditions. The response of NO_2 gas was 700%, which has high gas sensing selectivity characteristics compared to other gases. In air, photoelectrons generated by UV irradiation on the V_O -ZnO NW sensor combined with oxygen species and were trapped in V_O to produce oxygen species. Subsequently, NO_2 gas was injected, and the increased oxygen species interacted with the NO_2 species to promote NO_3^- production. As a result, the depletion width was thicker, inducing high resistance.

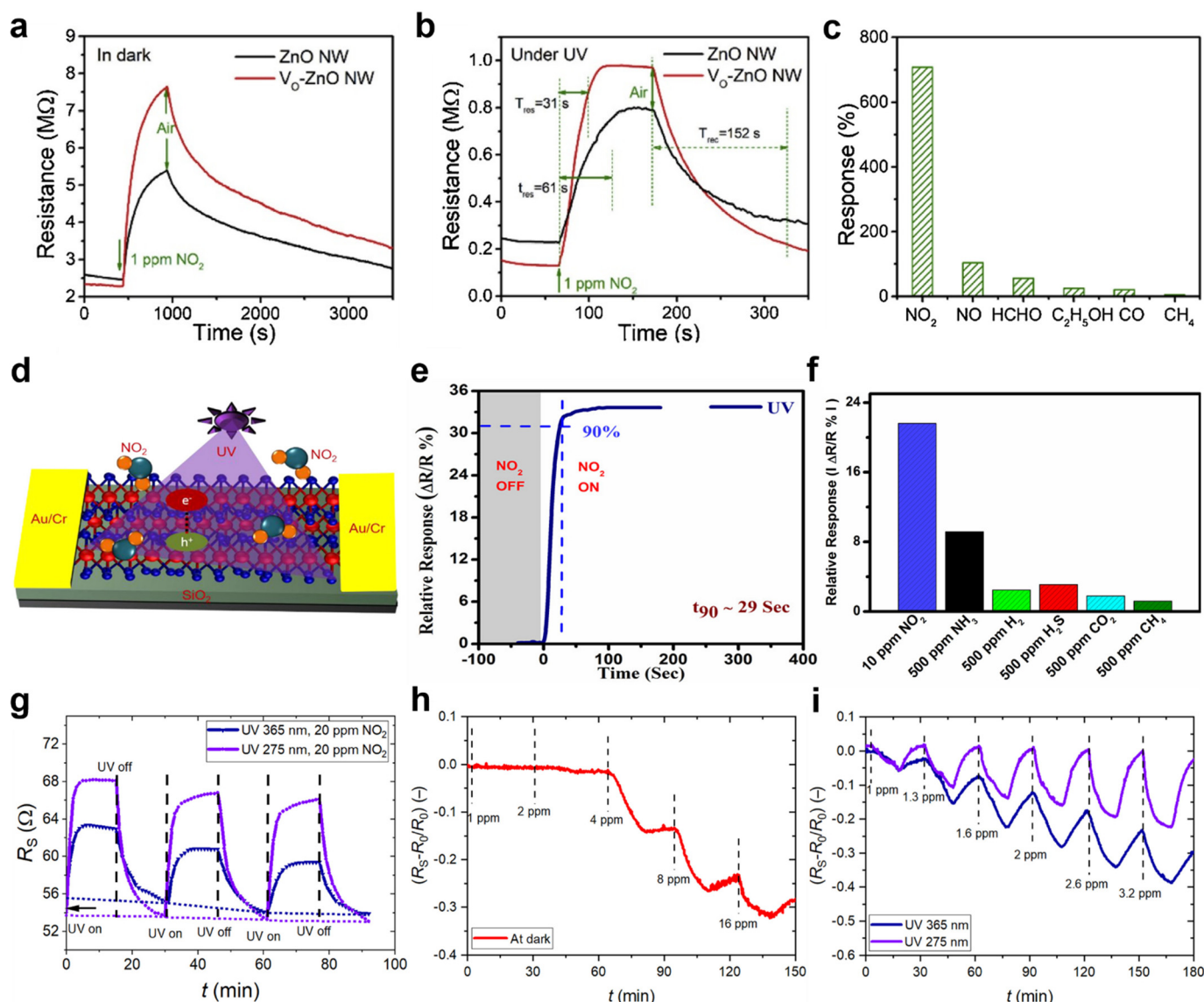


Figure 3. Resistance changes in the ZnO NW sensor and the Vo–ZnO NW sensor (a) under dark (b) under UV irradiation; (c) gas selectivity characteristics of the Vo–ZnO NW sensor (adapted from [87] with permission from the Elsevier B.V.); (d) schematic diagram of the MoS₂–based gas sensor; (e) response time of the MoS₂–based gas sensor under UV irradiation; (f) selectivity histogram of the MoS₂–based gas sensor (adapted from [88] with permission from the American Chemical Society); (g) response of the CNN sensor with UV lights irradiation ($\lambda = 365, 275$ nm); (h) response of the CNN sensor under the dark condition; (i) response of the CNN sensor under UV irradiation (adapted from [89] with permission from the Elsevier B.V.).

To fabricate the gas sensor, transition metal dichalcogenides (TMDs) were used, which have excellent electrical and optical characteristics. Kumar et al. demonstrated a MoS₂–based NO₂ gas detection at ambient temperature using UV light illumination [88]. MoS₂ was grown through the CVD process, and the annealing process was performed. Figure 3d presents a schematic diagram of the MoS₂–based gas sensor operating under UV irradiation ($\lambda = 365$ nm). The MoS₂–based gas sensor was fabricated by growing MoS₂ on SiO₂/Si substrates by CVD. The Au/Cr (200 nm/5 nm) electrodes were deposited by thermal evaporation, and the widths of the electrodes were 100 and 250 μ m, respectively. The response time of the MoS₂–based gas sensor to NO₂ gas under UV light irradiation conditions was investigated (Figure 3e). The MoS₂–based gas sensor was injected with 100 ppm NO₂ gas. The response time was defined as the time until the saturation of

the relative response reached 90% after the NO₂ gas was injected. The response time of the MoS₂-based gas sensor in UV conditions was 29 s, which was approximately 42 s faster than the gas response by thermal activation (100 °C). Figure 3f shows the relative responses of the MoS₂-based gas sensor to various gases. The relative response of the NO₂ gas measured was approximately 21%, which has the highest selectivity compared to other gases.

A gas sensor with a high surface-to-volume ratio was achieved using one-dimensional carbon nanotubes (CNT). Drozdowska et al. used a carbon nanotube network (CNN) to fabricate NO₂ gas sensors with a high surface-to-volume ratio [89]. The CNTs have p-type semiconductor characteristics and high sensitivity to gases owing to the large number of bonding sites on their large surface. The CNN is sensitive to UV light irradiation and improves response speed. The UV light used in this study has a wavelength of 365 nm and 275 nm, respectively, and can detect at least 1 ppm of NO₂. Figure 3g shows the response of the CNN gas sensor to 20 ppm NO₂ gas. The NO₂ gas response increases with the amount of UV light irradiated to the CNN gas sensor. Furthermore, the initial resistance of the CNN gas sensor increases as the UV-on and UV-off cycles are repeated. The response of the CNN sensor to various NO₂ gases was investigated. Figure 3h shows the NO₂ gas response of the CNN sensor in the dark. NO₂ gas concentrations below 4 ppm are difficult to detect in the dark. On the other hand, the CNN gas sensor irradiated with UV light improves the sensing performance to detect low concentrations of NO₂ gas, such as 1 ppm (Figure 3i). As a result, the UV irradiation increases the NO₂ gas response of the CNN sensor. The resistance of the CNN gas sensor increased when NO₂ was injected, and UV light irradiation increased the resistance change. UV-generated holes interact with negatively charged ions on the CNT surface, resulting in oxygen desorption. At this point, the lowered hole concentration reduces the conductivity of the CNN sensor. Additionally, the UV wavelength means that more energy is applied to the CNN sensor, resulting in the effective desorption of gas molecules, and accordingly, a rapid recovery of the CNN sensors was achieved.

2.3. UV-Activated Formaldehyde Gas Sensors

For enhancing the responsiveness of the gas sensor, a porous structure was used. Li et al. reported the formaldehyde (HCHO) gas sensor by loading Au on the porous octahedrons' (POHs) structured ZnO surface [90]. ZnO is an n-type metal oxide that has the advantages of being low-cost and nontoxic and is used as the core material of gas sensors. On the other hand, to improve the performance of ZnO-based gas sensors, operation at high temperatures leads to high power consumption. As a solution, UV light irradiation makes ZnO-based gas detectors operate at ambient temperature, but it has a low response. The porous structure was introduced into the MOS to improve the responsivity of the gas sensor due to the high surface-to-volume ratio. Furthermore, chemical catalytic materials, such as Au, are loaded into ZnO to produce a Schottky junction, leading to improved gas sensing performance. Figure 4a shows the HCHO gas response of a ZnO POH sensor and an Au-loaded ZnO POH sensor (Au-ZnO POH). The UV light used had a wavelength of 365 nm, and 50–800 ppm HCHO gas was investigated. The Au-ZnO POH sensor has more responsiveness for all concentrations of HCHO gas than the ZnO POH sensor. In particular, the responsiveness of 800 ppm HCHO gas doubled. In this way, the Au loading effect improves its response toward HCHO molecules. In addition, the selectivity of the Au-ZnO POH sensor was investigated. Figure 4b shows the responsiveness of the Au-ZnO POH sensor to various gases. Methanol, ethanol, acetone, benzene, and formaldehyde with a concentration of 400 ppm were assessed. The responses of the Au-ZnO POH sensor to all these gases were superior to those of the ZnO POH sensor. Figure 4c shows the resistance changes in the ZnO POH and Au-ZnO POH sensors exposed to the HCHO gas. The Au loading allows more oxygen molecules to be adsorbed onto the ZnO POH surface, leading to a thicker depletion layer resulting in high resistance.

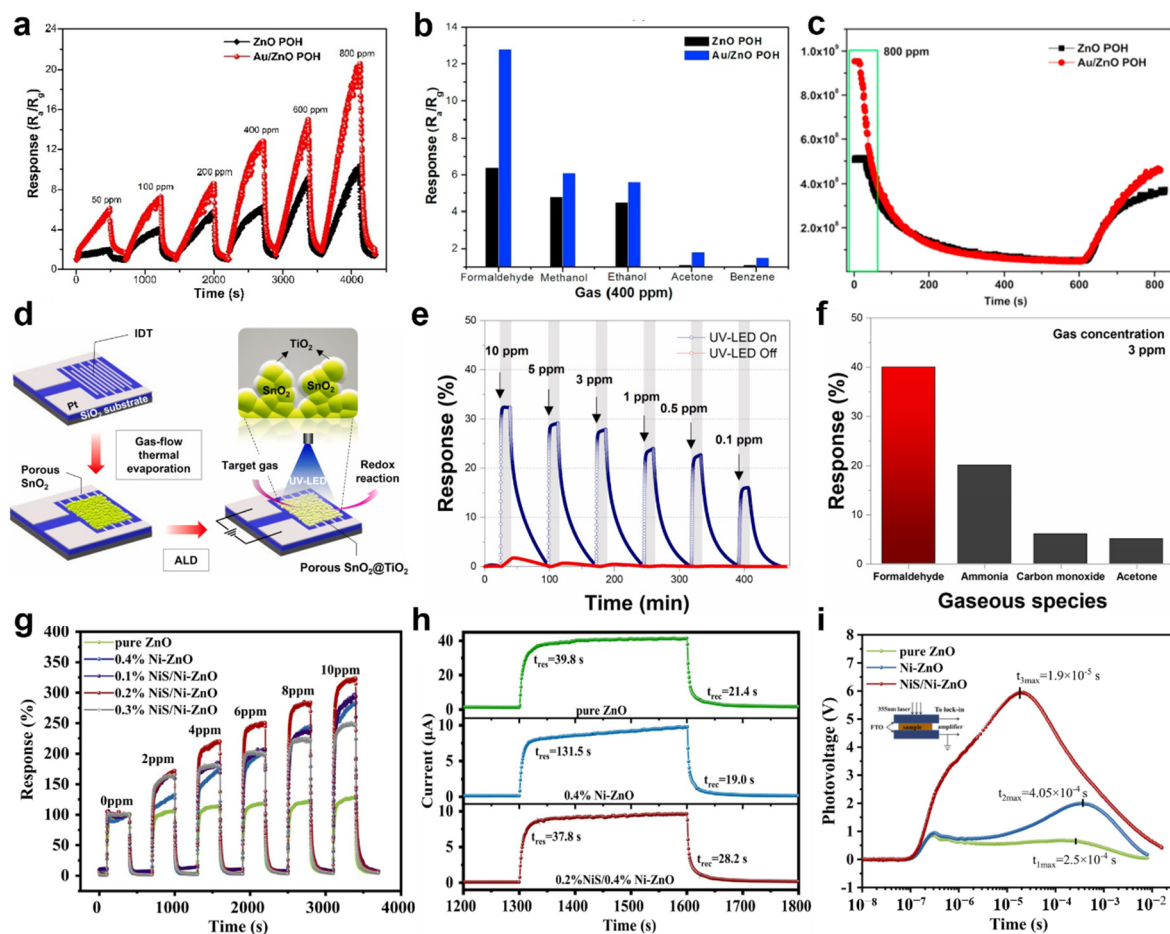


Figure 4. (a) Response of ZnO POH sensor and Au–ZnO POH sensor under UV irradiation; (b) response of the ZnO POH and Au–ZnO POH sensors to various gases; (c) actual resistance changes in the ZnO POH and Au–ZnO POH sensors (adapted from [90] with permission from the Elsevier B.V.); (d) schematic diagram of the SnO₂@TiO₂ sensor fabrication process; (e) response of the SnO₂@TiO₂ sensor in UV–on and UV–off; (f) selectivity characteristics of the SnO₂@TiO₂ sensor (adapted from [91] with permission from the Elsevier B.V.); (g) response of the pure ZnO, Ni–ZnO, and NiS/Ni–ZnO gas sensors to UV irradiation; (h) response time of the pure ZnO, Ni–ZnO, and NiS/Ni–ZnO gas sensors to HCHO gas; (i) spectrum of transient photovoltage (TPV) (adapted from [92] with permission from the Elsevier B.V.).

In 2021, Chang et al. produced a HCHO gas sensor based on the heterostructure of TiO₂ and SnO₂ to detect low HCHO gas concentrations [91]. The synergy between SnO₂ in a porous structure and TiO₂ as a photocatalytic material resulted in a high surface area that detected HCHO gas selectively, leading to an improved response of the gas sensor. Figure 4d shows the fabrication process of the SnO₂@TiO₂ gas sensor. Ti (10 nm) and Pt (150 nm) electrodes were deposited in an interdigitated shape on a SiO₂/Si substrate. Subsequently, SnO₂ and TiO₂ were deposited sequentially. SnO₂ has a nanoporous structure due to the kinetic energy of argon gas injected during the thermal evaporation process. Such a nanoporous structure can increase the response of the SnO₂@TiO₂ gas sensor because of its high surface–to–volume ratio and large surface area for activation. The TiO₂ with photocatalytic material was deposited using atomic layer deposition (ALD). Figure 4e shows the HCHO gas response characteristics of the SnO₂@TiO₂ sensor in UV–on and UV–off. The wavelength of the irradiated UV light was 365 nm, and the concentration of the injected HCHO gas was 0.1–10 ppm. The response of the SnO₂@TiO₂ sensor irradiated with UV–on was increased compared to the UV–off. The increased resistance change caused by UV light irradiation allows the sensor to detect lower HCHO gas concentrations.

In particular, the change in resistance to 0.1 ppm HCHO gas with UV–on increased by approximately 16% compared to UV–off. Figure 4f shows the selectivity of the SnO₂@TiO₂ sensor. Compared to ammonia, carbon monoxide, and acetone gas, the response to HCHO gas at 3 ppm was 40%. The electron–hole pairs generated by the UV produced reactive oxygen species on the TiO₂ surface. The injected HCHO molecules interacted with the adsorbed oxygen ions on the TiO₂ surface and released electrons. As a result, the released electrons accumulated in the TiO₂ conduction band and reduced the resistance.

To improve the responsiveness of a ZnO–based HCHO gas sensor, Yang et al. decorated nickel sulfide (NiS) nanomaterials onto Ni–doped ZnO [92]. The Ni–ZnO restrained the recombination of photo–generated electrons by UV light irradiation and increased carrier concentration. In addition, the NiS nanomaterials improved the response time of the NiS/Ni–ZnO gas sensors. Figure 4g shows the response of the HCHO gas range from 2 to 10 ppm with UV light irradiation ($\lambda = 365$ nm). The pure ZnO, Ni–ZnO, and NiS/Ni–ZnO gas sensors were compared to investigate the response of the HCHO gas. NiS decorating enhanced the response of the gas sensor. The response of the 0.4% Ni–ZnO gas sensor to 10 ppm of HCHO gas was 275%. On the other hand, the response of the 0.2% NiS/0.4% Ni–ZnO gas sensor was improved by 330%. Furthermore, the NiS improved the response time of the NiS/Ni–ZnO gas sensor. As shown in Figure 4h, the response time of the NiS/Ni–ZnO gas sensor was 37.8 s, which was significantly faster than the Ni–ZnO gas sensor with a response time of 131.5 s. Temporal photovoltage (TPV) characterizations were performed to investigate the transfer properties of photoexcited charge carriers (Figure 4i). The increased TPV response showed that the NiS/Ni–ZnO gas sensor has more photo–generated charges. In addition, the NiS/Ni–ZnO gas sensors have the fastest time to reach maximum TPV. In other words, the NiS decorated on Ni–ZnO improves the HCHO gas response time of the NiS/Ni–ZnO gas sensor by enhancing the separation and transmission efficiency of the photo–excited electrons and holes. UV light irradiation increased the change in resistance of the NiS/Ni–ZnO gas sensor. Oxygen in the air adsorbed to the surface of ZnO–based materials interacts with electrons in the ZnO conduction band promoted by UV light to generate oxygen ions. At this time, the Ni doping effect provided sites for trapping holes, enlarged oxygen ions adsorbed on the surface compared to pure ZnO. Oxygen ions adsorbed on the surface make the depletion layer of the NiS/Ni–ZnO gas sensor thicker. When HCHO gas was injected, the oxygen ions interacted with the HCHO molecule and generated electrons. The generated electrons were then transferred to the conduction band of the ZnO, increasing its conductivity.

2.4. UV–Activated Ammonia Oxide Gas Sensors

MOS and organic semiconductors were used to fabricate the ammonia (NH₃) gas sensor. Safe et al. produced an NH₃ gas sensor using a heterojunction of a p–type semiconductor polyaniline (PANI) and n–type semiconductor one–dimensional TiO₂ nanofibers [93]. PANI, with a porous morphology, detected NH₃ molecules selectively at room temperature, and TiO₂ has a photocatalytic function. The PANI/TiO₂ core–shell sensor, in which the two semiconductor materials were applied simultaneously, exhibited improved photocatalytic properties and selective NH₃ gas response in a UV light irradiation. The PANI/TiO₂ core–shell sensor was irradiated with UV at a wavelength of 365 nm to investigate the change in resistance. Figure 5a shows the resistance change in the sensor with a TiO₂ core created from a material containing a 30% anatase–70% rutile mixed crystal phase. The sensor shows improved photocatalytic characteristics compared to the sole rutile crystal phase. The PANI/TiO₂ core–shell sensor was exposed to 50 ppb to 40 ppm NH₃ gas, and the electrical response was measured. The PANI/TiO₂ core–shell sensor had a response time of 63 s and a recovery time of 37 s when 1 ppm of NH₃ gas was injected. Figure 5b shows the stability of the PANI/TiO₂ core–shell sensor measured at 15–day intervals. The response of 1 ppm NH₃ gas was measured under UV light irradiation. The gas sensor in which the core of TiO₂ has an anatase–rutile phase showed an approximately 22% decreased response when exposed to UV light because of the

reduced activity of the photocatalyst. In addition, the selective gas response performance for NH_3 gas increased when the PANI/ TiO_2 core–shell sensor was irradiated with UV light (Figure 5c). UV irradiation improved the response time and recovery time of the PANI/ TiO_2 core–shell sensor.

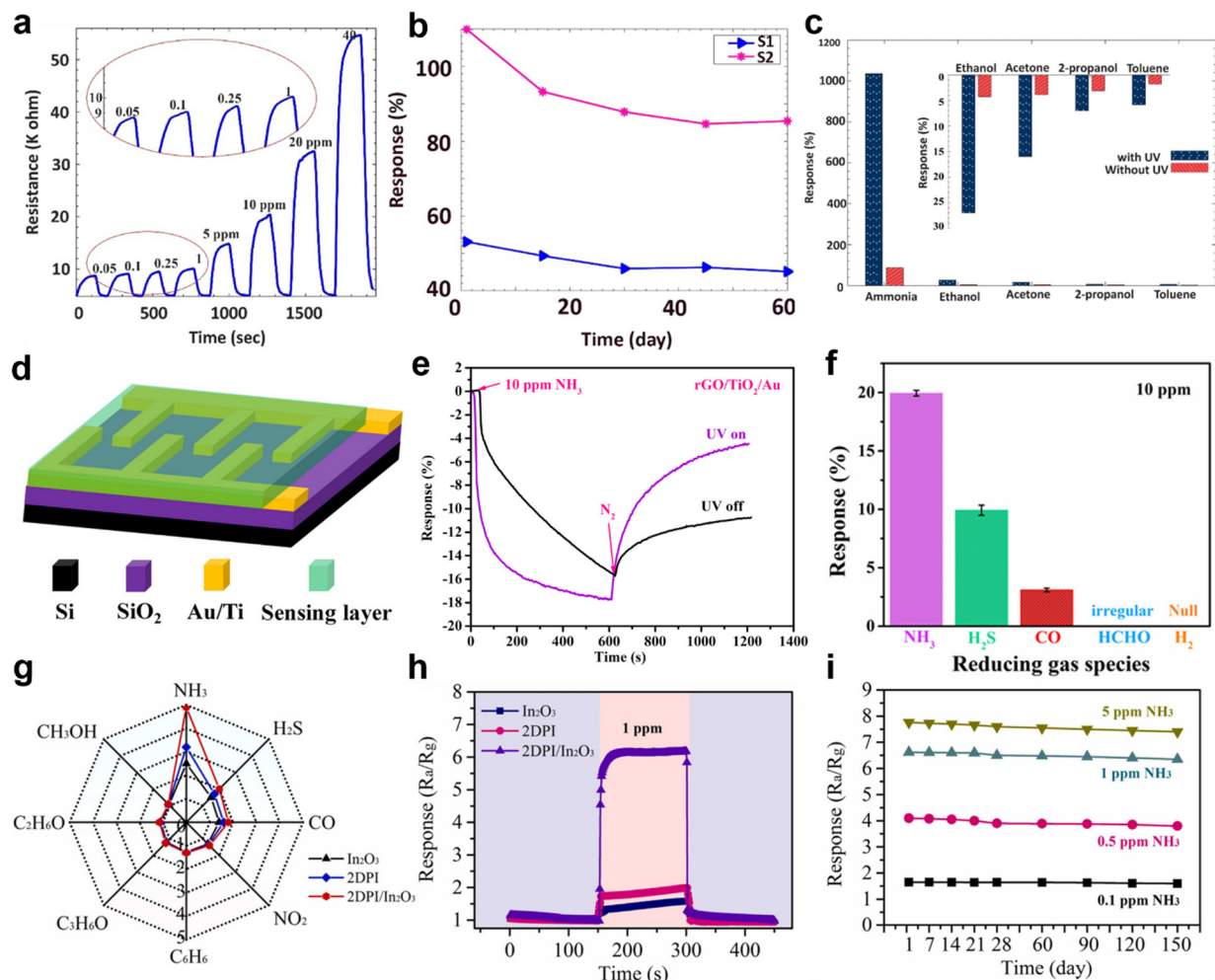


Figure 5. (a) Resistance change in the PANI/ TiO_2 core–shell sensor; (b) stability of the PANI/ TiO_2 core–shell sensor with UV irradiation; (c) selectivity characteristics of the PANI/ TiO_2 core–shell sensor (adapted from [93] with permission from the Elsevier B.V.); (d) schematic diagram of the $\text{rGO}/\text{TiO}_2/\text{Au}$ sensor; (e) response of the $\text{rGO}/\text{TiO}_2/\text{Au}$ sensor with UV–on and UV–off; (f) gas selectivity characteristics of the $\text{rGO}/\text{TiO}_2/\text{Au}$ sensor (adapted from [94] with permission from the American Chemical Society); (g) selectivity of the pure 2DPI, pure In_2O_3 , and the 2DPI/ In_2O_3 gas sensor under various gases; (h) response of the pure 2DPI, pure In_2O_3 , and the 2DPI/ In_2O_3 gas sensor with UV light irradiation; (i) long–term stability of the 2DPI/ In_2O_3 gas sensor (adapted from [95] with permission from the Elsevier B.V.).

In 2018, Zhou et al. first reported a UV–enhanced NH_3 detection sensor using graphene oxide nanosheets (rGO), TiO_2 NPs, and Au NPs [94]. The rGO acted as the template to attach the TiO_2 NPs and Au NPs and produced a high electron collector and transporter. The rGO with high conductivity detected changes in resistance effectively without heating. TiO_2 NPs are photocatalytic materials that interact with UV light and NH_3 molecules. Au NPs increase the sorption sites on the surface to detect sorption molecules and promote charge separation of electron–hole pairs generated by UV light. Figure 5d shows a schematic diagram of the $\text{rGO}/\text{TiO}_2/\text{Au}$ sensor. To fabricate the $\text{rGO}/\text{TiO}_2/\text{Au}$ sensor, Si/ SiO_2 was used for the substrate. Subsequently, Au (120 nm)/Ti (40 nm) electrodes

were formed into planar interdigital shapes, and a conventional photolithography and lift-off process was used for patterning. In addition, the width of the electrode was 50 μm . The synthesized rGO/TiO₂/Au solution was spray-coated on the prepared substrate and thermally treated in a vacuum oven. Figure 5e shows the NH₃ gas response characteristics of the rGO/TiO₂/Au sensor under UV irradiation ($\lambda = 365\text{ nm}$) and dark conditions. The response to NH₃ gas is higher under UV irradiation than in the dark. The NH₃ gas response of the rGO/TiO₂/Au sensor with UV irradiation increased to 2.1% compared to the dark conditions. Additionally, response speed and recovery level were enhanced by 234 s and 43%, respectively. In addition, the selective characteristics of the rGO/TiO₂/Au sensor were investigated. Figure 5f shows the gas response to NH₃, H₂S, CO, HCHO, and H₂ gases. The selectivity for NH₃ gas was approximately two times higher than that of the other gases. UV light irradiation enhanced the NH₃ gas detection performance of the rGO/TiO₂/Au sensor. In the dark, electrons from the rGO/TiO₂/Au sensor flow from TiO₂ NPs to Au NPs, producing a large-area depletion layer in rGO/TiO₂ before being exposed to NH₃ molecules. UV light irradiation induces more electrons to flow into Au NPs, resulting in a thicker depletion region. In addition, exposure of NH₃ molecules to the rGO/TiO₂/Au sensor interacts with more free electrons generated by UV light, resulting in an enhanced response.

The response of the gas sensor was improved by synthesizing organic materials and MOS. Yang et al. demonstrated an NH₃ gas sensor using a composite material of two-dimensional polyimide (2DPI) and indium oxide (In₂O₃) [95]. Under UV light irradiation, the response of the 2DPI/In₂O₃ gas sensor was enhanced three times compared to the response of the gas sensor using only 2DPI or In₂O₃. 2DPI with photocatalytic characteristics promotes electron-hole separation and improves the response of In₂O₃-based gas sensors under UV illumination. The In₂O₃ with three-dimensional layered increases the adsorption sites through self-assembly properties. The NH₃ gas response of the 2DPI/In₂O₃ gas sensor and pure 2DPI and In₂O₃ were compared. The response of the 2DPI/In₂O₃ gas sensor exposed to 10 ppm NH₃ gas was approximately 6.9, which was higher than that of pure 2DPI and In₂O₃ gas sensors. The enhanced response of NH₃ was due to the generated heterojunction between 2DPI and In₂O₃. Figure 5g shows the response of the 2DPI/In₂O₃ gas sensor to various gases. The 2DPI/In₂O₃ gas sensor has a higher NH₃ gas selectivity characteristic than the two reference sensors mentioned above. Figure 5h shows the response of the pure 2DPI and In₂O₃ gas sensors and the 2DPI/In₂O₃ gas sensor under UV ($\lambda = 365\text{ nm}$) irradiation conditions. The 2DPI/In₂O₃ gas sensor was exposed to 1 ppm NH₃ gas. The responses of the pure 2DPI and pure In₂O₃ gas sensors were 1.6 and 2.1, respectively. On the other hand, the response of the 2DPI/In₂O₃ gas sensor under UV light irradiation was 6.5, which was 3.66 times higher than the response in the dark. Figure 5i shows the long-term stability of the 2DPI/In₂O₃ gas sensor for ammonia gas detection. Over 150 days, 0.1, 0.5, 1, and 5 ppm of NH₃ gas could be detected without degradation. The heterojunction of the 2DPI/In₂O₃ gas sensor improved the electrical conductivity. In Fermi level equilibrium, the electrons of 2DPI move into In₂O₃. In addition, oxygen ions are formed through oxygen in the air and free electrons. Subsequently, NH₃ molecules with injected oxygen ions interact to reduce the sensor resistance. The energy of UV light is 3.4 eV, which is higher than the bandgap of the 2DPI/In₂O₃ composites (2.95 eV). Thus, photo-generated electrons from UV light cause more oxygen ion production, making the depletion layer smaller.

3. Visible-Activated Gas Sensors

3.1. Visible-Activated Nitric Oxide Gas Sensors

In 2019, Chinh et al. reported a ZnO-based NO gas sensor loaded with an Au NP catalyst [96]. The energy of visible light irradiated to Au NPs reduced the barrier energy of ZnO, activating the adsorption and desorption of NO and oxygen molecules. A 2.5 mm \times 2.5 mm Al₂O₃ substrate was prepared to fabricate the Au/ZnO gas sensor (Figure 6a). First, finger-shaped Au electrodes were deposited on the substrate. Diethyl

zinc [$\text{Zn}(\text{C}_2\text{H}_5)_2$] and H_2O were then flowed alternately through ALD to deposit a ZnO thin film. Subsequently, an annealing treatment was performed at 500°C for two hours. The Au NPs were loaded on the ZnO thin film by immersing the films in an Au colloidal solution and annealing them at 500°C . The wavelengths of the light-emitting diode (LED) used to measure the Au/ZnO gas sensor were ultraviolet ($\lambda = 382\text{ nm}$), blue ($\lambda = 439\text{ nm}$), and green ($\lambda = 525\text{ nm}$), and light with an intensity of $0.76\text{ mW}/\text{cm}^2$ was irradiated. Figure 6b shows the response of the Au/ZnO gas sensor to various wavelengths of light when exposed to 10 ppm NO gas. The Au/ZnO gas sensor exhibited the strongest response of more than 12 in blue light irradiation. In addition, the resistance of the Au/ZnO gas sensor was increased because the Schottky contact was bent more. Figure 6c shows the selectivity of the Au/ZnO gas sensor. The response of 150 ppm of NH_3 , H_2S , H_2 , CO, and CH_4 gases was investigated. On the other hand, the responses to other gases were lower than that of 10 ppm NO gas.

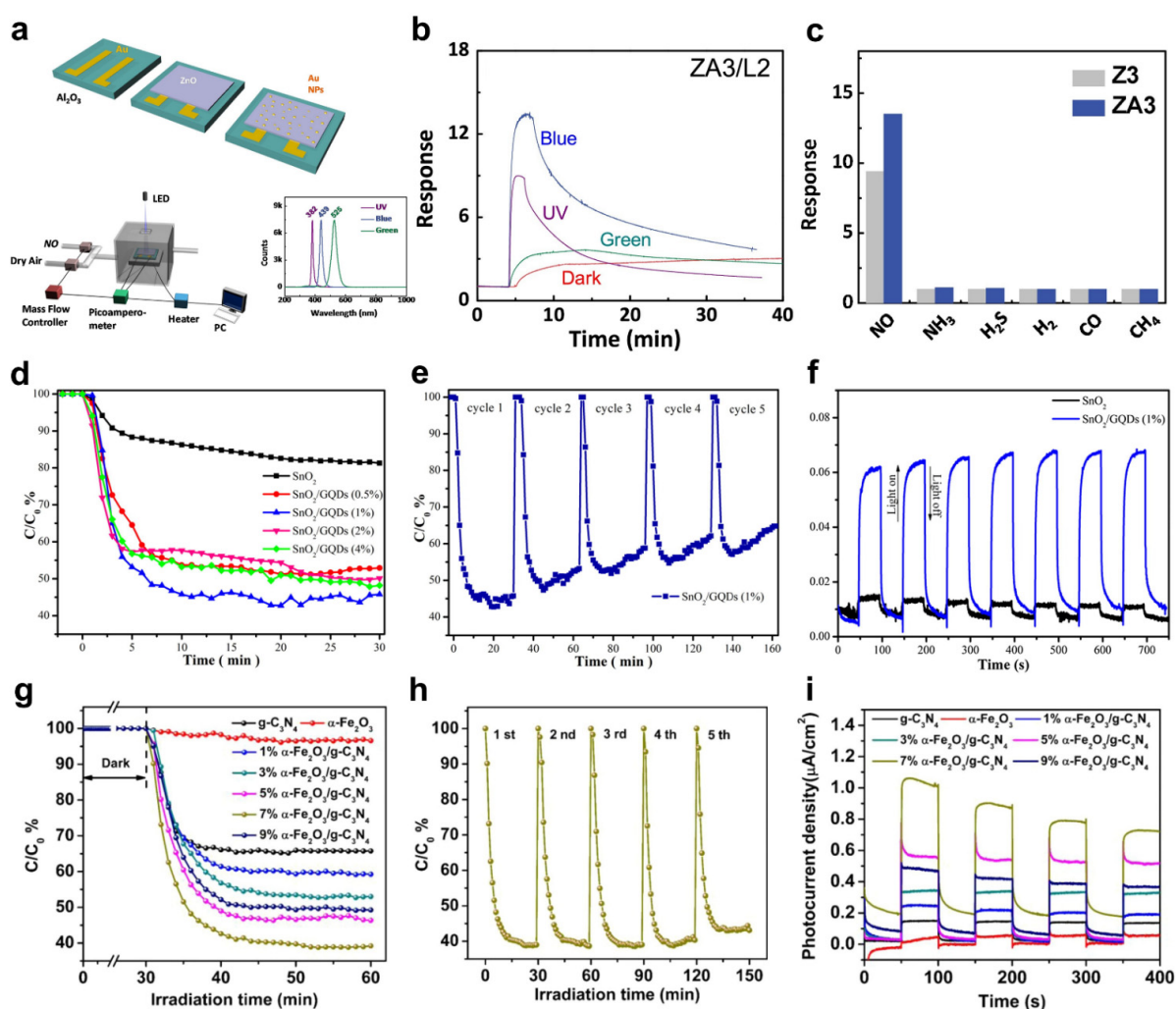


Figure 6. (a) Fabrication process of the Au/ZnO gas sensor; (b) response of the Au/ZnO gas sensor with various light irradiation (UV, blue, green); (c) selectivity characteristics of the Au/ZnO gas sensor (adapted from [96] with permission from the Elsevier B.V.); (d) photocatalytic spectrum of SnO_2/GQDs under visible light irradiation; (e) recycling test for of SnO_2/GQDs with visible light irradiation; (f) photocurrent density of the pure SnO_2 and SnO_2/GQDs (adapted from [97] with permission from the Elsevier B.V.); (g) photocatalytic performances of $\alpha\text{-Fe}_2\text{O}_3/\text{g-C}_3\text{N}_4$ sensors with different composite ratios in removing NO gas; (h) recycling test for 7% SnO_2/GQDs sensor with visible light irradiation; (i) photocurrent response of pure $\alpha\text{-Fe}_2\text{O}_3$, $\text{g-C}_3\text{N}_4$, and $\alpha\text{-Fe}_2\text{O}_3/\text{g-C}_3\text{N}_4$ (adapted from [98] with permission from the Elsevier B.V.).

To fabricate NO gas sensors with improved reactivity under visible light irradiation, Xie et al. used tin oxide (SnO_2) and graphene quantum dots (GQDs) [97]. SnO_2 , an n-type MOS, has a bandgap of 3.60 eV and is used as a core material in gas sensors because of its excellent electrical and optical characteristics. Nevertheless, it is difficult to use visible light for a SnO_2 -based sensor with a wide bandgap. Hence, SnO_2 and GQDs with a narrow bandgap material were combined to fabricate high-response gas sensors. The GQDs improved the charge separation efficiency when irradiated with visible light. The photocatalytic characteristics were investigated according to the GQD content. Figure 6d shows the photocatalytic spectrum for the NO gas under visible light irradiation. All samples were exposed to 600 ppb of NO gas, and the adsorption-desorption state was equilibrated by exposure to the NO gas for 30 minutes before visible light irradiation. The NO removal rate with only SnO_2 was 18%, whereas it increased dramatically when GQDs were deposited on SnO_2 . The rate of NO gas removal reached 57% when the amount of GQDs was 1%. On the other hand, excessive deposition of GQDs reduces light efficiency because it blocks the active site of SnO_2 . Figure 6e shows a cycle test for the NO gas under visible light irradiation. During the five cycles, the degradation product accumulated and deteriorated the photoactivity. Figure 6f shows the photocurrent densities of the pure SnO_2 and SnO_2 /GQDs under visible light irradiation. The improved charge separation efficiency due to QGD increased the response of the SnO_2 /GQDs sensor under visible light illumination.

In 2021, Geng et al. reported a heterojunction-structured NO gas sensor using carbon nitride (g- C_3N_4) and hematite (α - Fe_2O_3) [98]. g- C_3N_4 is a photocatalytic material but shows poor performance for NO removal gas due to rapid electron-hole recombination and low light harvesting ability. The photocatalytic efficiency was increased by combining α - Fe_2O_3 with g- C_3N_4 to achieve a heterojunction structure of the Z-scheme. The presented 2D/2D structure has a high interfacial area and active sites for interacting with NO molecules and effectively absorbing visible light to promote charge separation and transport. Figure 6g shows the photocatalytic performance of the α - Fe_2O_3 /g- C_3N_4 sensors with different composite ratios of NO removal. The α - Fe_2O_3 /g- C_3N_4 sensor was irradiated with visible light using a Xe lamp with a 400 nm cutoff filter applied. The NO gas removal performance of pure α - Fe_2O_3 and g- C_3N_4 was 3.4% and 34.2%, respectively. On the other hand, the NO gas degradation efficiency increased when the heterojunction was formed. Overall, the charge separation efficiency increased with increasing α - Fe_2O_3 content. The highest NO gas degradation efficiency of 60.8% was observed when the α - Fe_2O_3 content was 7%. Figure 6h shows the NO gas removal rate of 7% α - Fe_2O_3 /g- C_3N_4 over five cycles. The optimized α - Fe_2O_3 content barely changed the NO removal efficiency and stabilized the sensor. Figure 6i shows the photocurrent response of various samples. Similarly, pure α - Fe_2O_3 and g- C_3N_4 had the lowest photocurrent density. However, 7% α - Fe_2O_3 /g- C_3N_4 had the highest photocurrent density. An appropriate α - Fe_2O_3 content produces a g- C_3N_4 active area with enhanced NO gas degradation efficiency and photocurrent density.

3.2. Visible-Activated Nitric Dioxide Gas Sensors

In_2O_3 nanowires (NWs) synthesized by electrospinning improve the responsivity of gas sensors with a high surface area. Zhang et al. produced a NO_2 gas sensor based on In_2O_3 nanowires (NWs) [99]. In_2O_3 is an n-type MOS with a bandgap of 2.8 eV and high conductivity that exhibits responsivity and selectivity to NO_2 gas. The In_2O_3 NWs have a high surface area and a loose arrangement, which promotes the interaction between the NO_2 molecules and oxygen species. Defects in the In_2O_3 NWs and oxygen species absorbed on the surface increase the responsivity to NO_2 gas. On the other hand, the In_2O_3 NWs gas sensor has a long recovery time in the dark. To achieve a rapid recovery time, irradiating visible light promotes the removal of adsorbed NO_2 gas from the In_2O_3 NWs gas sensor. Figure 7a shows the response of the In_2O_3 NWs gas sensor when exposed to 5 ppm of NO_2 gas. Visible light has a wavelength range of 400 to 700 nm and was irradiated with

an intensity of 4.58 mW/cm^2 . The resistance was restored to 90% of the initial value in approximately 20 s when the In_2O_3 NWs gas sensor was irradiated by visible light, and at the same time, the NO_2 gas flow was stopped. In addition, repeated tests were performed to confirm the stability of the In_2O_3 NWs gas sensor (Figure 7b). The In_2O_3 NWs gas sensor was controlled in visible light, and the changed resistance reached the initial value during five cycles without deterioration. Figure 7c shows the selectivity characteristics of the In_2O_3 NWs gas sensor. The response to 5 ppm NO_2 gas was highest at 740. On the other hand, the responses to ethanol, formaldehyde, and toluene gas were negligible. In addition, NO , NH_3 , and H_2S gases showed stronger responses than volatile organic compounds (VOCs) but were significantly lower than NO_2 gas. The initial resistance of the In_2O_3 NWs gas sensor is determined by the oxygen species adsorbed on the surface. When the In_2O_3 NWs gas detectors were exposed to NO_2 gas, oxygen-related gases on the surface and electrons extracted from the conduction band of In_2O_3 NWs interacted and increased the resistance. On the other hand, photons generated by visible light irradiation desorb the oxygen ions from the surface. Thus, the released electrons were transported to In_2O_3 nanowires, reducing the resistance.

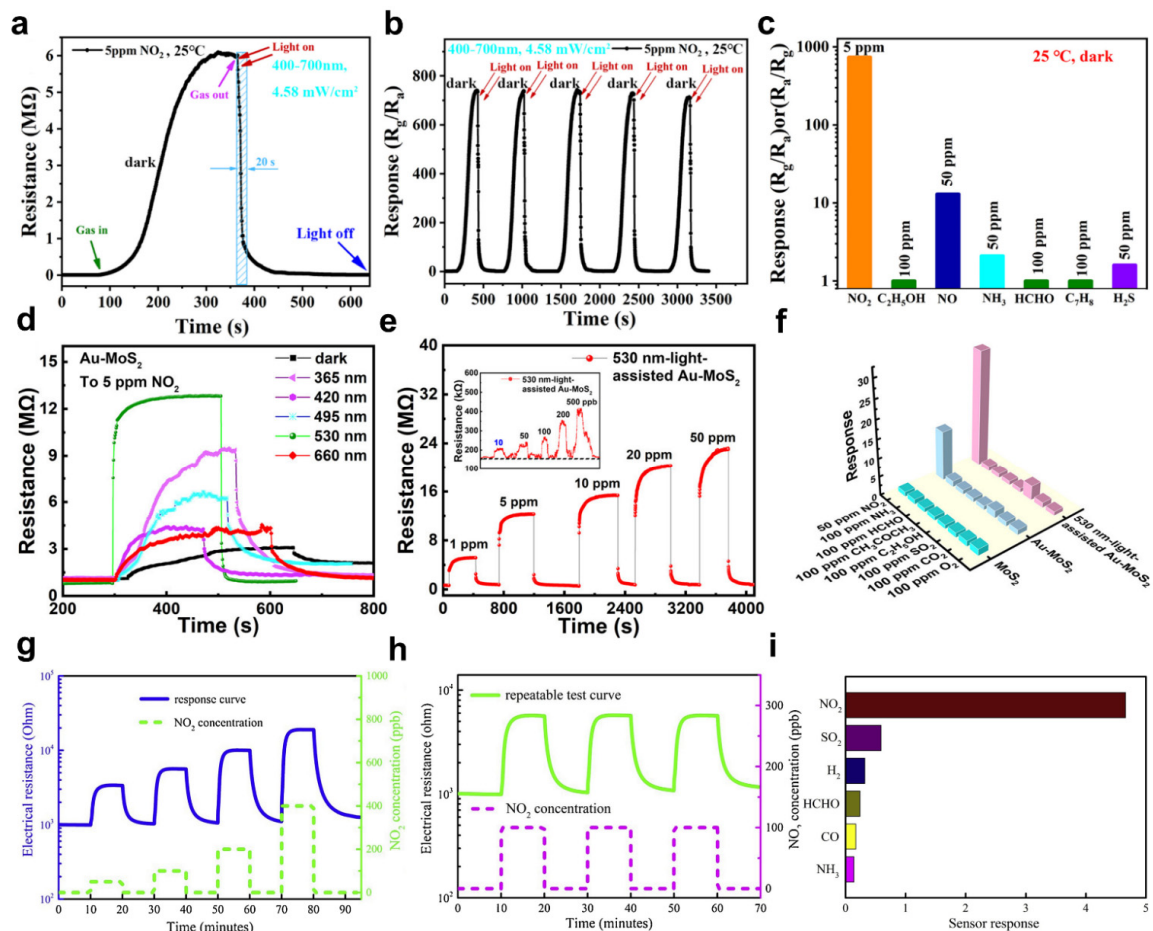


Figure 7. (a) Response of the In_2O_3 NWs gas sensor with visible light irradiation; (b) stability characteristics of the In_2O_3 NWs gas sensor; (c) selectivity characteristics of the In_2O_3 NWs gas sensor (adapted from [99] with permission from the Elsevier B.V.); (d) response of the Au-MoS_2 gas sensor with UV and visible light; (e) response of the Au-MoS_2 gas sensor with various NO_2 gas concentration; (f) selectivity characteristics of the Au-MoS_2 gas sensor (adapted from [100] with permission from the American Chemical Society); (g) electrical resistance response of the rGO@ZnO sensor with white light illumination; (h) repeated NO_2 gas response of the rGO@ZnO sensor; (i) selectivity characteristics of the rGO@ZnO sensor (adapted from [101] with permission from the Elsevier B.V.).

To enhance the detection limit of a MoS₂-based NO₂ gas sensor, Chen et al. loaded Au NPs on MoS₂ to use the localized surface plasmon resonance (LSPR) effect [100]. The decorated Au NPs irradiated with optimized light, the strong absorption of light, and the enhanced electromagnetic near-field due to the LSPR effect increase the light absorption efficiency of MoS₂. In addition, Au-MoS₂, with its high surface-to-volume ratio structure, provides more opportunity to interact with NO₂ gas. Figure 7d shows the response of the Au-MoS₂ gas sensor to the NO₂ gas with various wavelengths of light ($\lambda = 365, 420, 495, 530,$ and 660 nm) irradiated. The power of the visible light source irradiated to the Au-MoS₂ gas sensor was the same as 10 W, and 5 ppm NO₂ gas was injected. Visible light at 530 nm was optimized for NO₂ gas detection. The frequency of visible light at 530 nm and the vibration frequency of Au NPs correspond. Au NPs absorb more photon energy because of the matched frequency. As a result, the Au-MoS₂ gas sensor has an LSPR effect with strong absorption for 530 nm visible light. In addition, the response to different concentrations of NO₂ gas was investigated (Figure 7e). The Au-MoS₂ gas sensor detected 10 ppb to 50 ppm NO₂ gas, and the irradiated light improved the detection limit of NO₂ gas. Figure 7f shows the selectivity of the pure MoS₂ and Au-MoS₂ gas sensors in the dark and under visible light illumination. The pure MoS₂-based gas sensor showed the weakest response to all gases. On the other hand, the response to NO₂ gas increased when loaded with Au NPs. In addition, irradiation with 530 nm visible light further enhanced the gas response to NO₂ gas.

In 2021, Geng et al. synthesized reduced graphene (rGO) and the used oxygen-deficient zinc oxide (ZnO_{1-x}) composites using hydrothermal methods. Based on these combinations, they produced an NO₂ gas detector operating at ambient temperature [101]. Donor defects generated during synthesis narrow the bandgap of ZnO, allowing it to respond to visible light. In addition, the rGO effectively absorbs light with its large surface area and electron mobility. The p-n junction produced at the ZnO interface attached to the rGO enhanced the NO₂ sensing response to white light. Figure 7g shows the electrical resistance response of the rGO@ZnO sensor to 50 to 400 ppb of NO₂ gas. The rGO@ZnO sensor was irradiated with white light with an intensity of 0.15 W/cm². The rGO@ZnO sensor showed improved responsivity compared to the pure ZnO sensor. The pure ZnO sensor had a response of 0.19 at 50 ppb NO₂ gas, while the rGO@ZnO sensor showed a response of 2.31. The increased response to low-concentration NO₂ gas improved the detection limit of the rGO@ZnO sensor. Figure 7h shows the response to the 100 ppb NO₂ gas repeated test. The rGO@ZnO sensor under white light irradiation showed repeated sensing without significant degradation. In addition, the selectivity characteristics of the rGO@ZnO sensor were investigated (Figure 7i). The concentrations of SO₂, CO, and NH₃ gases injected into the rGO@ZnO sensor were 100 ppm. In addition, 400 ppm H₂ gas and 10 ppm HCHO gas were injected. Finally, the concentration of NO₂ gas was 100 ppb, which was the lowest concentration but led to the strongest response.

3.3. Visible-Activated Formaldehyde Gas Sensors

In 2021, Song et al. produced an HCHO gas detector using P-type material, HoFeO₃ NPs, with high responsivity in light at various wavelengths ($\lambda = 365, 470, 530,$ and 660 nm) [102]. In particular, the HoFeO₃ gas sensor showed the most enhanced response to red light ($\lambda = 660$ nm). Figure 8a shows the HCHO gas response of the HoFeO₃ gas sensor in the dark under and various light illuminations. The HoFeO₃ gas detectors were exposed to 100 ppb to 100 ppm HCHO gas. The lowest detection limit of the HoFeO₃ gas sensor was 0.5 ppm, and the response was 0.64. On the other hand, the response to HCHO gas was improved when the HoFeO₃ gas sensor was irradiated with red light. Figure 8b shows the response of the HoFeO₃ gas sensor to red light irradiation. Compared to the dark condition, the response to HCHO gas improved under red light irradiation, and the response was 1.9 when exposed to 80 ppb HCHO gas. The selectivity of the HoFeO₃ gas sensor was investigated (Figure 8c). The HCHO, C₂H₆O, CH₃COCH₃, NH₃, and CH₃OH gases with concentrations of 100 ppm were injected into the HoFeO₃ gas sensor. In particular, the

HCHO gas showed a high response when irradiated with 660 nm and 365 nm light. In addition, the HoFeO₃ gas sensor had a strong response to NH₃. The HoFeO₃ gas sensor showed decreased resistance with NH₃ gas but increased resistance when exposed to HCHO gas. Thus, the two gases could be distinguished owing to their opposite tendency to change the resistance.

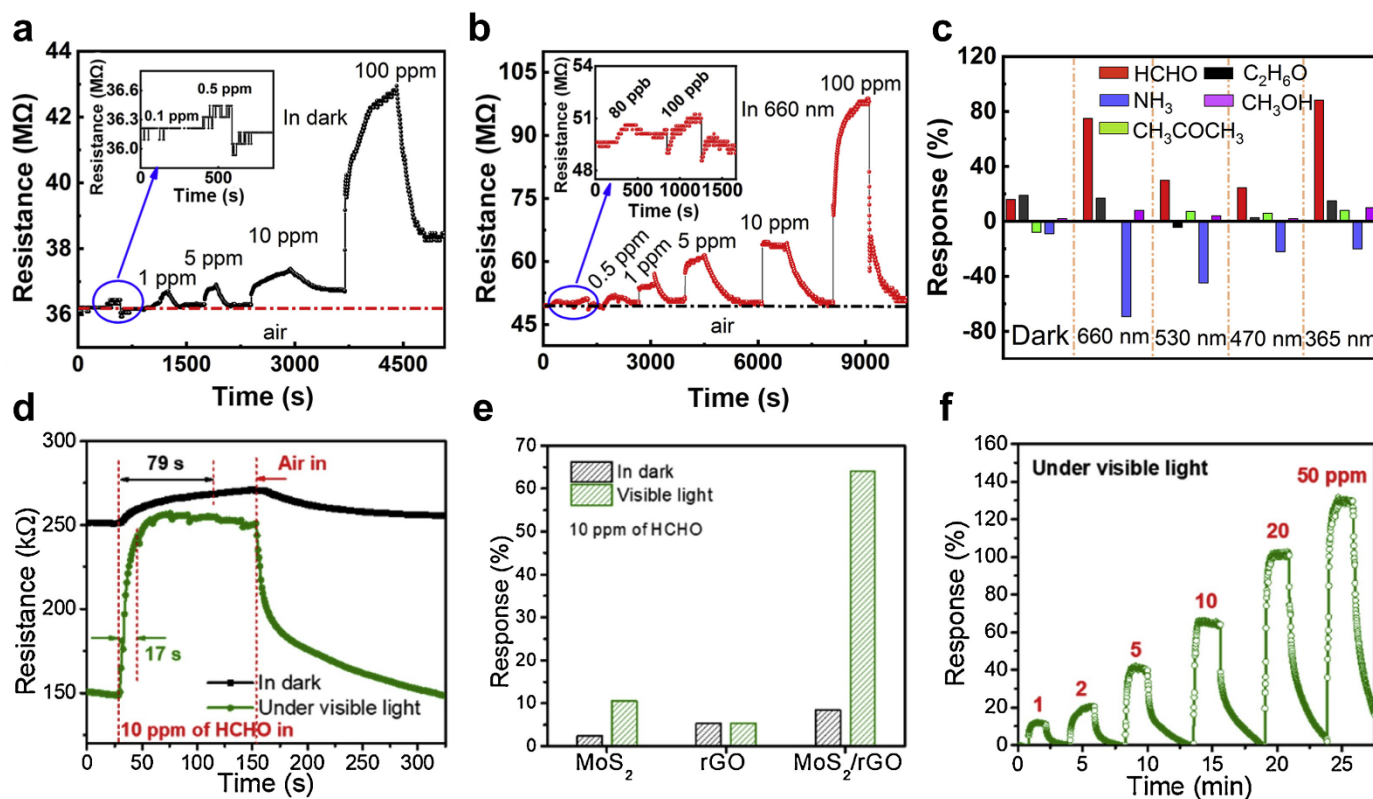


Figure 8. (a) Response of the HoFeO₃ gas sensor under dark and various visible light; (b) response of the HoFeO₃ gas sensor under red light irradiation; (c) selectivity characteristics of the HoFeO₃ gas sensor (adapted from [102] with permission from the Elsevier B.V.); (d) response of the MoS₂/rGO hybrid gas sensor in the dark condition and visible light irradiation; (e) responses of pure MoS₂, rGO, and MoS₂/rGO hybrid gas sensors; (f) response of the MoS₂/rGO hybrid gas sensor to 1–50 ppm HCHO gas (adapted from [103] with permission from the Elsevier B.V.).

The synergy of TMDs and graphene improved HCHO detection performance under visible light irradiation. In 2020, Wang et al. reported a MoS₂/rGO-based HCHO gas sensor [103]. MoS₂ acts as a photocatalyst material and oxidizes HCHO gas to CO₂ and H₂O when irradiated with visible light. In addition, rGO induces efficient charge separation. Figure 8d shows the response of the MoS₂/rGO hybrid gas sensor irradiated with visible light ($\lambda > 420$ nm) to 10 ppm HCHO gas. In addition, the responsivity under dark conditions was measured to compare to visible light irradiation conditions. When irradiated with visible light, the response time of the MoS₂/rGO hybrid gas sensor was 17 s, which is approximately 62 s less than in the dark condition. In addition, the resistance to HCHO gas increased. The initial resistance of the MoS₂/rGO hybrid gas sensor under visible light irradiation was 149 kΩ, which increased by 262 kΩ upon exposure to HCHO gas, resulting in an improved response of 64%. On the other hand, the response to HCHO gas was improved by 8.5% under dark conditions. The sensing responses of pure MoS₂, rGO, and MoS₂/rGO hybrid gas sensors were compared (Figure 8e). The response under dark and visible light conditions was compared with 10 ppm of injected HCHO gas. Although pure MoS₂ and rGO gas sensors have less than approximately 12% response, the MoS₂/rGO hybrid gas sensor with both materials applied has more than 60% response in visible light.

Figure 8f shows the response of the MoS₂/rGO hybrid gas sensor to exposure to 1 to 50 ppm HCHO gas. The MoS₂/rGO hybrid gas sensor exhibited a 12.6% response to 1 ppm of HCHO gas and 126.8% at 50 ppm.

3.4. Visible–Activated Ammonia Gas Sensors

In 2021, Huang et al. demonstrated a copper phthalocyanine–loaded zinc oxide (CuPc/ZnO)–based NH₃ gas sensor fabricated using a microwave–assisted hydrothermal synthesis method [104]. The responsivity of the CuPc/ZnO gas sensor with NH₃ gas was improved under red light irradiation ($\lambda = 600$ nm to 622 nm). The red–light irradiation effect promoted the desorption of oxygen on the ZnO surface, making the depletion layer thin. In addition, the photoelectrons generated by red light increased the electron concentration in ZnO, resulting in more oxygen ions that interact with the NH₃ molecules. Figure 9a shows the NH₃ gas response of the CuPc/ZnO gas sensor and the pure ZnO gas sensor. The concentration of injected NH₃ gas was 80 ppm, and the red light had an intensity of 0.15 W/cm². The pure ZnO gas sensor and the CuPc/ZnO gas sensor showed a further decrease in resistance when irradiated with red light than in the dark. On the other hand, the CuPc/ZnO gas sensor showed improved response and recovery times, as well as a response to NH₃ gas compared to the pure ZnO gas sensor (Figure 9b). The red–light illumination effect reduced the barrier height of the CuPc/ZnO gas sensor to enhance the electron mobility. The response time and recovery time values of the pure ZnO were measured at 31 s and 18 s, respectively. On the other hand, the CuPc/ZnO gas sensor exhibited a response time value of 20 s and a recovery time value of 10 s. Figure 9c shows the response behavior of the CuPc/ZnO gas sensor and the pure ZnO gas sensor to various gases. The selectivity of CH₃OH, C₂H₅OH, C₃H₅OH, H₂, CO, and CH₄ at 80 ppm was investigated. The response of the CuPc/ZnO gas sensor irradiated with red light to NH₃ gas was approximately 12, whereas the responses to the remaining gases were less than five.

For achieving high responsivity of NH₃ gas sensor, Shao et al. used silver phosphate (Ag₃PO₄) as a photocatalytic [105]. The Ag₃PO₄ NPs have efficient separation of electron–hole pairs with visible light illumination. The calculated bandgap and intrinsic absorption long wavelength limit of Ag₃PO₄ NPs synthesized by the precipitation method was 2.24 eV and 554 nm, respectively, which is less energy than the white LED with a wavelength range of 440 nm to 470 nm. Figure 9d shows the response of the Ag₃PO₄ NPs gas sensor to NH₃ gas with concentrations ranging from 10 to 300 ppm. Dark1 and Light1 indicate the responses of the Ag₃PO₄ NPs gas sensor to NH₃ gas with and without visible light illumination, respectively. Owing to the visible light activated Ag₃PO₄ NPs, the resistance change in the Ag₃PO₄ NPs gas sensor was larger under visible light illumination. In addition, when the Ag₃PO₄ NPs were exposed to light, they could corrode and generate metal silver on the surface, affecting the gas sensor’s performance. Dark 2 is the response of the Ag₃PO₄ NPs gas sensor in the dark, which was previously exposed to visible light to NH₃ gas. The response of Dark 2 was similar that in Dark 1 because of the suppressed photocorrosion of Ag₃PO₄ by adjusting the visible light exposure time. The LR is the calculated Ag₃PO₄ NPs gas sensor response under visible light without NH₃ gas. Figure 9e shows the selectivity characteristics of the Ag₃PO₄ NPs gas sensor. The Ag₃PO₄ NPs gas sensor was exposed to IPA, methanol, ethanol, gases, and NH₃ at 100 ppm each. The response of the Ag₃PO₄ NPs gas sensor to NH₃ gas was highly selective, 1.55 and 1.8 in the dark and visible light conditions, respectively. In addition, the response of mixed NH₃–based gases were investigated (Figure 9f). The Ag₃PO₄ NPs gas sensor has strong selectivity for NH₃ molecules as a result of its response to NH₃ based mixed gases.

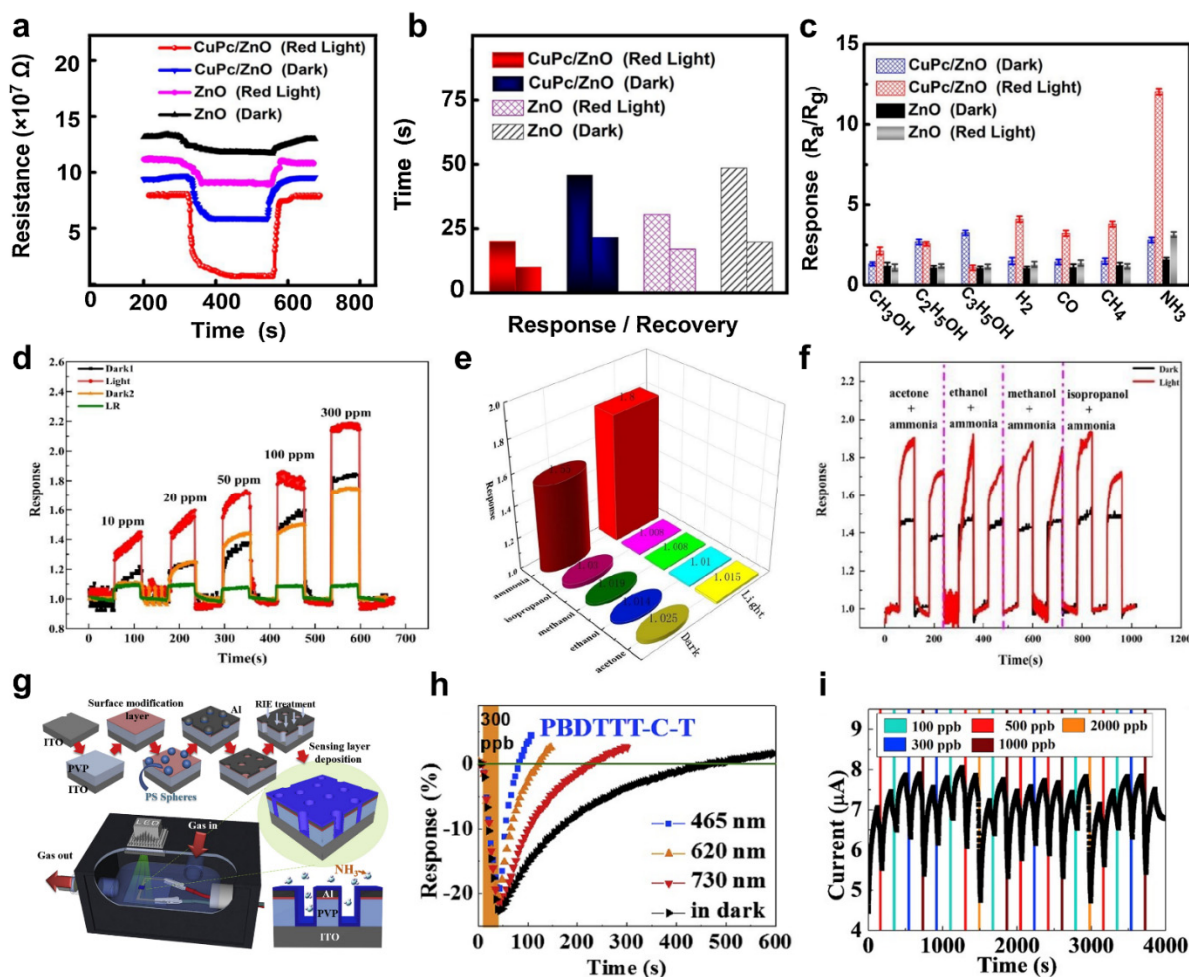


Figure 9. (a) Response of the CuPc/ZnO gas sensor and the pure ZnO gas sensor in dark and under red light irradiation; (b) response and recovery time of the CuPc/ZnO gas sensor and the pure ZnO gas sensor under dark and red light irradiation; (c) selectivity characteristics of the CuPc/ZnO gas sensor (adapted from [104] with permission from the Elsevier B.V.); (d) response of the Ag_3PO_4 NPs gas sensor; (e) selectivity characteristics of the Ag_3PO_4 NPs gas sensor; (f) response of the mixed NH_3 -based gas (adapted from [105] with permission from the John Wiley and Sons); (g) fabrication process of the PBDTT-C-T gas sensor and the NH_3 gas detection system; (h) response of the PBDTT-C-T gas sensor; (i) stability of the PBDTT-C-T gas sensor (adapted from [106] with permission from the Elsevier B.V.).

Visible light was irradiated to shorten the recovery time of organic material-based gas sensors. Lin et al. reported a NH_3 gas detector with a vertical diode by using poly[[4,8-bis[5-(2-ethylhexyl)-2-thienyl]benzo[1,2-b:4,5-b']dithiophene-2,6-diyl][2-(2ethyl-1-oxohexyl)thieno[3,4-b]thiophenediyl]] (PBDTT-C-T) [106]. The PBDTT-C-T gas detector based on the organic materials was irradiated with various wavelengths of visible light to compensate for the slow recovery time. On the other hand, the recovery time was improved when the PBDTT-C-T gas sensor was irradiated with blue light because of the current compensation effect. Figure 9g shows the fabrication process of the PBDTT-C-T gas sensor and the NH_3 gas detection system. ITO with improved surface hydrophilic characteristics through the oxygen plasma treatment was used as a substrate. Subsequently, poly(4-vinylphenol) (PVP) for the insulating layer was deposited by spin coating. Poly(3-hexylthiophene-2,5-diyl) (P3HT) was spin-coated for the adhesion of polystyrene (PS) nano-spheres. The prepared samples were immersed in a PS solution to form polystyrene (PS) nano-spheres. Al was deposited over the entire surface using the evaporation method, and the PS spheres were removed using 3M Scotch tape

to induce porous patterning on the sample. The exposed PVP was removed by oxygen plasma etching. Finally, PBDTTT–C–T was deposited using the blade coating method. The PBDTTT–C–T gas sensor was mounted in an opaque box, and the wavelengths of the LED used were 465, 620, and 730 nm. Figure 9h shows the response of the PBDTTT–C–T gas sensor to 300 ppb of NH₃ gas. After NH₃ gas was injected into the PBDTTT–C–T gas sensor for 30 s, it was irradiated with the LED. As a result, the recovery time was improved when the PBDTTT–C–T gas sensor was irradiated with LED light. In addition, the enhanced response to light at 465 nm was attributed to the stronger irradiance than the other two LEDs. Figure 9i shows the response of the PBDTTT–C–T gas sensor to NH₃ at concentrations from 100 to 2000 ppb. The stability of the PBDTTT–C–T gas sensor was confirmed by performing at least three tests with different NH₃ gas concentrations. Table 1 summarizes the sensing performance of photo-activated gas sensors for NO, NO₂, HCHO, and NH₃ based on UV and visible light.

Table 1. Comparison of sensing performance of the photo-activated gas sensor.

Materials	Light	Target Gas	Limit of Detection	Sensitivity	Ref
TiO ₂ @NGQDs	UV ($\lambda = 365$ nm)	Nitric oxide	10 ppm	~31.1% at 100 ppm	[85]
Cu–TCA/TiNCs	UV ($\lambda = 365$ nm)	Nitric oxide	140 ppb	~124% at 50 ppm	[86]
ZNO NW	UV ($\lambda = 325$ nm)	Nitric dioxide	20 ppb	~708% at 1 ppm	[87]
MoS ₂	UV ($\lambda = 365$ nm)	Nitric dioxide	5 ppm	~3% at 100 ppm	[88]
CNT	UV ($\lambda = 365, 275$ nm)	Nitric dioxide	1 ppm	N/A	[89]
Au–ZnO POH	UV ($\lambda = 365$ nm)	Formaldehyde	50 ppm	~7.6 at 100 ppm	[90]
SnO ₂ @TiO ₂	UV ($\lambda = 365$ nm)	Formaldehyde	100 ppb	~32.5% at 10 ppm	[91]
NiS/Ni–ZnO	UV ($\lambda = 365$ nm)	Formaldehyde	2 ppm	~330% at 10 ppm	[92]
PANI/TiO ₂	UV ($\lambda = 365$ nm)	Ammonia	50 ppb	~109.87% at 1 ppm	[93]
rGO/TiO ₂ /Au	UV ($\lambda = 365$ nm)	Ammonia	2 ppm	~8.9% at 50 ppm	[94]
2DPI/In ₂ O ₃	UV ($\lambda = 365$ nm)	Ammonia	50 ppb	~6.5 at 1 ppm	[95]
Au/ZnO	Vis ($\lambda = 382, 439, 525$ nm)	Nitric oxide	1 ppm	~ 12 at 10 ppm, blue	[96]
SnO ₂ /GQDs	Vis ($\lambda \geq 420$ nm)	Nitric oxide	600 ppb	N/A	[97]
α -Fe ₂ O ₃ / g-C ₃ N ₄	Vis ($\lambda \geq 400$ nm)	Nitric oxide	600 ppb	N/A	[98]
In ₂ O ₃ NW	Vis ($\lambda = 400$ to 700 nm)	Nitric dioxide	10 ppb	~ 750% at 5 ppm	[99]
Au/MoS ₂	Vis ($\lambda = 530$ nm)	Nitric dioxide	10 ppb	~8.1 at 1 ppm	[100]
rGO@ZnO	Vis, white LED	Nitric dioxide	50 ppb	~2.31 at 50 ppb	[101]
HoFeO ₃	Vis ($\lambda = 660$ nm)	Formaldehyde	80 ppb	~78% at 100 ppm	[102]
MoS ₂ /rGO	Vis ($\lambda > 420$ nm)	Formaldehyde	20 ppb	~64% at 10 ppm	[103]
CuPc/ZnO	Vis ($\lambda = 600$ to 622 nm)	Ammonia	800 ppb	~12 at 80 ppm	[104]
Ag ₃ PO ₄ NP	Vis ($\lambda = 400$ to 800 nm)	Ammonia	10 ppm	~45% at 10 ppm	[105]
PBDTTT–C–T	Vis ($\lambda = 465, 620, 730$ nm)	Ammonia	100 ppb	~22 at 300 ppb, blue	[106]

4. Conclusions

This review reported various strategies for producing gas detectors activated by ultraviolet and visible light that have been reported in recent years. Research on photo-activated gas detectors using metal oxide semiconductors, TMDs, and carbon nanotubes has been reported. Techniques, such as porous structures, heterojunctions, and surface defects, improve the responsivity, selectivity, response, and recovery time of photo-activated gas detectors. In addition, photo-activated gas detectors are classified according to the type of detectable gas, such as nitric oxide, nitric dioxide, formaldehyde, and ammonia gas. Photo-activated

gas detectors, with external light illumination, replaced conventional high-temperature gas detectors, providing a technological foundation for low-power consumption and miniaturization. On the other hand, despite these advantages, photo-activated gas sensing technology still has technical barriers to overcome, and technology development strategies for advancing high-performance light-activated gas detectors are needed.

1. Photo-activated gas detectors use a specific wavelength of light to increase selectivity for a target gas. However, most of the photoactive gas detector performance has been reported in an environment where the variables are controlled, such as temperature and humidity. Therefore, to commercialize photoactive gas detectors in the industry, measurements should be performed in an environment with complex variables, including detecting a target gas contained in a mixed gas.
2. The photo-activated gas detection system should reduce its weight and size for portability and miniaturization. The presence of light sources that irradiate ultraviolet or visible light has expanded the use of photo-activated gas detection systems. In addition, the integration of existing systems, such as computers and smartphones, should be considered. Therefore, it is necessary to re-examine the photo-activated gas detection system using a new structural design.
3. The sustainability and stability of photoactive detectors need to be reviewed further. Gas detectors are attracting attention as a safety system in various fields, such as factories and hospitals. To monitor a gas in real time, it is necessary to ensure the overall durability and reliability of the photoactive gas detectors.
4. The presence or absence of a disease could be diagnosed through the concentration of a target gas detected in human exhalation. On the other hand, it is necessary to detect low concentrations of gases precisely to distinguish between healthy and diseased people. The photoactive gas detectors for diagnosing disease require an improved response to low-concentration gases.

In spite of the aforementioned technical limitations, research and technological development of photo-activated gas detectors are actively progressing. Photo-activated gas detectors have potential advantages for gas detection and are believed to be core electronics for industrial stabilization in the future.

Author Contributions: H.Y. initiated the research project. D.H.L. performed the literature survey and research analysis. All authors have read and agreed to the published version of the manuscript.

Funding: This research was supported by the National Research Foundation of Korea (NRF) grant funded by the Korean Government (MSIT) (NRF-2022R1C1C1004590). This work was supported in part by the Gachon University Research Fund of 2021 (GCU-202106380001).

Institutional Review Board Statement: Not applicable.

Informed Consent Statement: Not applicable.

Conflicts of Interest: The authors declare no conflict of interest.

References

1. Kaniyoor, A.; Jafri, R.I.; Arockiadoss, T.; Ramaprabhu, S. Nanostructured Pt decorated graphene and multi walled carbon nanotube based room temperature hydrogen gas sensor. *Nanoscale* **2009**, *1*, 382–386. [[CrossRef](#)] [[PubMed](#)]
2. Lupan, O.; Chai, G.; Chow, L. Novel hydrogen gas sensor based on single ZnO nanorod. *Microelectron. Eng.* **2008**, *85*, 2220–2225. [[CrossRef](#)]
3. Wong, Y.M.; Kang, W.P.; Davidson, J.L.; Wisitsora-At, A.; Soh, K.L. A novel microelectronic gas sensor utilizing carbon nanotubes for hydrogen gas detection. *Sens. Actuators B Chem.* **2003**, *93*, 327–332. [[CrossRef](#)]
4. Xing, X.; Chen, T.; Zhao, R.; Wang, Z.; Wang, Y. A low temperature butane gas sensor used Pt nanoparticles-modified AZO macro/mesoporous nanosheets as sensing material. *Sens. Actuators B Chem.* **2018**, *254*, 227–238. [[CrossRef](#)]
5. Liu, X.; Pan, K.; Wang, L.; Dong, C.; Xiao, X.; Wang, Y. Butane detection: W-doped TiO₂ nanoparticles for a butane gas sensor with high sensitivity and fast response/recovery. *RSC Adv.* **2015**, *5*, 96539–96546. [[CrossRef](#)]
6. Kim, J.C.; Jun, H.K.; Huh, J.-S.; Lee, D.D. Tin oxide-based methane gas sensor promoted by alumina-supported Pd catalyst. *Sens. Actuators B Chem.* **1997**, *45*, 271–277. [[CrossRef](#)]

7. Waitz, T.; Wagner, T.; Sauerwald, T.; Kohl, C.; Tiemann, M. Ordered mesoporous In_2O_3 : Synthesis by structure replication and application as a methane gas sensor. *Adv. Funct. Mater.* **2009**, *19*, 653–661. [[CrossRef](#)]
8. Niu, L.; Luo, Y.; Li, Z. A highly selective chemical gas sensor based on functionalization of multi-walled carbon nanotubes with poly(ethylene glycol). *Sens. Actuators B Chem.* **2007**, *126*, 361–367. [[CrossRef](#)]
9. Sholehah, A.; Karmala, K.; Huda, N.; Utari, L.; Septiani, N.L.W.; Yulianto, B. Structural effect of ZnO-Ag chemoresistive sensor on flexible substrate for ethylene gas detection. *Sens. Actuators A Phys.* **2021**, *331*, 112934. [[CrossRef](#)]
10. Seddik, B.; Salima, B.; Houda, G. Fe doped ZnO nanostructures prepared via sol-gel dip-coating technique for iso-butane (i-C₄H₁₀) sensing. *Mater. Today Commun.* **2021**, *29*, 102805. [[CrossRef](#)]
11. Guillén-Bonilla, H.; Flores-Martínez, M.; Rodríguez-Betancourt, V.-M.; Guillén-Bonilla, A.; Reyes-Gómez, J.; Gildo-Ortiz, L.; de la Luz Olvera Amador, M.; Santoyo-Salazar, J. A novel gas sensor based on MgSb₂O₆ nanorods to indicate variations in carbon monoxide and propane concentrations. *Sensors* **2016**, *16*, 177. [[CrossRef](#)]
12. Morán-Lázaro, J.P.; Guillén-López, E.S.; López-Urias, F.; Muñoz-Sandoval, E.; Blanco-Alonso, O.; Guillén-Bonilla, H.; Guillén-Bonilla, A.; Rodríguez-Betancourt, V.M.; Sanchez-Tizapa, M.; Olvera-Amador, M.d.l.l. Synthesis of ZnMn₂O₄ nanoparticles by a microwave-assisted colloidal method and their evaluation as a gas sensor of propane and carbon monoxide. *Sensors* **2018**, *18*, 701. [[CrossRef](#)] [[PubMed](#)]
13. Latyshev, V.M.; Berestok, T.O.; Opanasyuk, A.S.; Korniyushchenko, A.S.; Perekrestov, V.I. Nanostructured ZnO films for potential use in LPG gas sensors. *Solid State Sci.* **2017**, *67*, 109–113. [[CrossRef](#)]
14. Shinde, V.R.; Gujar, T.P.; Lokhande, C.D.; Mane, R.S.; Han, S.-H. Use of chemically synthesized ZnO thin film as a liquefied petroleum gas sensor. *Mater. Sci. Eng. B* **2007**, *137*, 119–125. [[CrossRef](#)]
15. Fu, Y.; Nie, Y.; Zhao, Y.; Wang, P.; Xing, L.; Zhang, Y.; Xue, X. Detecting liquefied petroleum gas (LPG) at room temperature using ZnSnO₃/ZnO nanowire piezo-nanogenerator as self-powered gas sensor. *ACS Appl. Mater. Interfaces* **2015**, *7*, 10482–10490. [[CrossRef](#)] [[PubMed](#)]
16. Wang, L.; Wang, S.; Xu, M.; Hu, X.; Zhang, H.; Wang, Y.; Huang, W. A Au-functionalized ZnO nanowire gas sensor for detection of benzene and toluene. *Phys. Chem. Chem. Phys.* **2013**, *15*, 17179–17186. [[CrossRef](#)]
17. Li, Z.; Huang, Y.; Zhang, S.; Chen, W.; Kuang, Z.; Ao, D.; Liu, W.; Fu, Y. A fast response & recovery H₂S gas sensor based on α -Fe₂O₃ nanoparticles with ppb level detection limit. *J. Hazard. Mater.* **2015**, *300*, 167–174. [[PubMed](#)]
18. Vessally, E.; Behmagham, F.; Massoumi, B.; Hosseinian, A.; Edjlali, L. Carbon nanocone as an electronic sensor for HCl gas: Quantum chemical analysis. *Vacuum* **2016**, *134*, 40–47. [[CrossRef](#)]
19. Aguir, K.; Lemire, C.; Lollman, D.B.B. Electrical properties of reactively sputtered WO₃ thin films as ozone gas sensor. *Sens. Actuators B Chem.* **2002**, *84*, 1–5. [[CrossRef](#)]
20. Da Silva, L.F.; Catto, A.C.; Avansi, W.; Cavalcante, L.S.; Andrés, J.; Aguir, K.; Mastelaro, V.R.; Longo, E. A novel ozone gas sensor based on one-dimensional (1D) α -Ag₂WO₄ nanostructures. *Nanoscale* **2014**, *6*, 4058–4062. [[CrossRef](#)]
21. Zhou, Q.; Zeng, W.; Chen, W.; Xu, L.; Kumar, R.; Umar, A. High sensitive and low-concentration sulfur dioxide (SO₂) gas sensor application of heterostructure NiO-ZnO nanodisks. *Sens. Actuators B Chem.* **2019**, *298*, 126870. [[CrossRef](#)]
22. Luo, Y.; Zhang, D.; Fan, X. Hydrothermal Fabrication of Ag-Decorated MoSe₂/Reduced Graphene Oxide Ternary Hybrid for H₂S Gas Sensing. *IEEE Sens. J.* **2020**, *20*, 13262–13268. [[CrossRef](#)]
23. Leidinger, M.; Rieger, M.; Sauerwald, T.; Alépée, C.; Schütze, A. Integrated pre-concentrator gas sensor microsystem for ppb level benzene detection. *Sens. Actuators B Chem.* **2016**, *236*, 988–996. [[CrossRef](#)]
24. Thota, C.; Modigunta, J.K.R.; Reddeppa, M.; Park, Y.H.; Kim, H.; Kang, H.; Kokkiligadda, S.; Lee, S.; Murali, G.; Park, S.Y. Light stimulated room-temperature H₂S gas sensing ability of Cl-doped carbon quantum dots supported Ag nanoparticles. *Carbon N. Y.* **2022**, *196*, 337–346. [[CrossRef](#)]
25. Reddeppa, M.; Park, B.-G.; Murali, G.; Choi, S.H.; Chinh, N.D.; Kim, D.; Yang, W.; Kim, M.-D. NO_x gas sensors based on layer-transferred n-MoS₂/p-GaN heterojunction at room temperature: Study of UV light illuminations and humidity. *Sens. Actuators B Chem.* **2020**, *308*, 127700. [[CrossRef](#)]
26. Mahalingam, A.; Naayagi, R.T.; Mastorakis, N.E. Design and implementation of an economic gas leakage detector. *Recent Res. Appl. Electr. Comput. Eng.* **2012**, *3*, 20–24.
27. Brunelli, D.; Rossi, M. Enhancing lifetime of WSN for natural gas leakages detection. *Microelectron. J.* **2014**, *45*, 1665–1670. [[CrossRef](#)]
28. Aalsalem, M.Y.; Khan, W.Z.; Gharibi, W.; Khan, M.K.; Arshad, Q. Wireless Sensor Networks in oil and gas industry: Recent advances, taxonomy, requirements, and open challenges. *J. Netw. Comput. Appl.* **2018**, *113*, 87–97. [[CrossRef](#)]
29. Suma, V.; Shekar, R.R.; Akshay, K.A. Gas leakage detection based on IOT. In Proceedings of the 2019 3rd International conference on Electronics, Communication and Aerospace Technology (ICECA), Coimbatore, India, 2–14 June 2019; IEEE: New York, NY, USA, 2019; pp. 1312–1315.
30. Rostrup-Nielsen, J.R. Production of synthesis gas. *Catal. Today* **1993**, *18*, 305–324. [[CrossRef](#)]
31. Galvita, V.V.; Semin, G.L.; Belyaev, V.D.; Semikolenov, V.A.; Tsiakaras, P.; Sobyenin, V.A. Synthesis gas production by steam reforming of ethanol. *Appl. Catal. A Gen.* **2001**, *220*, 123–127. [[CrossRef](#)]
32. York, A.P.E.; Xiao, T.; Green, M.L.H.; Claridge, J.B. Methane oxyforming for synthesis gas production. *Catal. Rev.* **2007**, *49*, 511–560. [[CrossRef](#)]

33. Raju, A.S.K.; Park, C.S.; Norbeck, J.M. Synthesis gas production using steam hydrogasification and steam reforming. *Fuel Process. Technol.* **2009**, *90*, 330–336. [[CrossRef](#)]
34. Lee, J.; Choi, N.J.; Lee, H.K.; Kim, J.; Lim, S.Y.; Kwon, J.Y.; Lee, S.M.; Moon, S.E.; Jong, J.J.; Yoo, D.J. Low power consumption solid electrochemical-type micro CO₂ gas sensor. *Sens. Actuators B Chem.* **2017**, *248*, 957–960. [[CrossRef](#)]
35. Fergus, J.W. Materials for high temperature electrochemical NO_x gas sensors. *Sens. Actuators B Chem.* **2007**, *121*, 652–663. [[CrossRef](#)]
36. Pang, X.; Shaw, M.D.; Gillot, S.; Lewis, A.C. The impacts of water vapour and co-pollutants on the performance of electrochemical gas sensors used for air quality monitoring. *Sens. Actuators B Chem.* **2018**, *266*, 674–684. [[CrossRef](#)]
37. Serafini, M.; Mariani, F.; Gualandi, I.; Decataldo, F.; Possanzini, L.; Tessarolo, M.; Fraboni, B.; Tonelli, D.; Scavetta, E. A wearable electrochemical gas sensor for ammonia detection. *Sensors* **2021**, *21*, 7905. [[CrossRef](#)]
38. Suresh, M.; Vasa, N.J.; Agarwal, V.; Chandapillai, J. UV photo-ionization based asymmetric field differential ion mobility sensor for trace gas detection. *Sens. Actuators B Chem.* **2014**, *195*, 44–51.
39. Pyo, S.; Lee, K.; Noh, T.; Jo, E.; Kim, J. Sensitivity enhancement in photoionization detector using microelectrodes with integrated 1D nanostructures. *Sens. Actuators B Chem.* **2019**, *288*, 618–624. [[CrossRef](#)]
40. Zhu, H.; She, J.; Zhou, M.; Fan, X. Rapid and sensitive detection of formaldehyde using portable 2-dimensional gas chromatography equipped with photoionization detectors. *Sens. Actuators B Chem.* **2019**, *283*, 182–187. [[CrossRef](#)]
41. Li, M.W.-H.; Ghosh, A.; Sharma, R.; Zhu, H.; Fan, X. Integrated microfluidic helium discharge photoionization detectors. *Sens. Actuators B Chem.* **2021**, *332*, 129504. [[CrossRef](#)]
42. Vyas, J.C.; Katti, V.R.; Gupta, S.K.; Yakhmi, J. V A non-invasive ultrasonic gas sensor for binary gas mixtures. *Sens. Actuators B Chem.* **2006**, *115*, 28–32. [[CrossRef](#)]
43. Minglei, S.; Xiang, L.; Changping, Z.; Jiahua, Z. Gas concentration detection using ultrasonic based on wireless sensor networks. In Proceedings of the 2nd International Conference on Information Science and Engineering, Hangzhou, China, 4–6 December 2010; IEEE: New York, NY, USA, 2010; pp. 2101–2106.
44. Costa, M.M.; Freire, R.C.S.; Villanueva, J.M.M.; Martins, V.S.G. Concentration H₂ measurement and uncertainty analysis using ultrasonic transducer. In Proceedings of the 2012 IEEE International Instrumentation and Measurement Technology Conference Proceedings, Graz, Austria, 13–16 May 2012; IEEE: New York, NY, USA, 2012; pp. 763–767.
45. Ding, X.; Shi, Y.; Sun, H.; Ding, X. A dual-frequency phase-difference method for ultrasonic hydrogen-concentration detection. *Rev. Sci. Instrum.* **2021**, *92*, 84901. [[CrossRef](#)] [[PubMed](#)]
46. Chintoanu, M.; Ghita, A.; Aciu, A.; Pitl, G.; Costiug, S.; Cadar, S.; Ferenczi, L.; Cordos, E. Methane and carbon monoxide gas detection system based on semiconductor sensor. In Proceedings of the 2006 IEEE International Conference on Automation, Quality and Testing, Robotics, Cluj-Napoca, Romania, 25–28 May 2006; IEEE: New York, NY, USA, 2006; Volume 2, pp. 208–211.
47. Zhang, J.; Qin, Z.; Zeng, D.; Xie, C. Metal-oxide-semiconductor based gas sensors: Screening, preparation, and integration. *Phys. Chem. Chem. Phys.* **2017**, *19*, 6313–6329. [[CrossRef](#)] [[PubMed](#)]
48. Li, B.; Zhou, Q.; Peng, S.; Liao, Y. Recent advances of SnO₂-based sensors for detecting volatile organic compounds. *Front. Chem.* **2020**, *8*, 321. [[CrossRef](#)]
49. Kang, Y.; Yu, F.; Zhang, L.; Wang, W.; Chen, L.; Li, Y. Review of ZnO-based nanomaterials in gas sensors. *Solid State Ionics* **2021**, *360*, 115544. [[CrossRef](#)]
50. Tang, H.; Prasad, K.; Sanjines, R.; Levy, F. TiO₂ anatase thin films as gas sensors. *Sens. Actuators B Chem.* **1995**, *26*, 71–75. [[CrossRef](#)]
51. Wan, Q.; Li, Q.H.; Chen, Y.J.; Wang, T.-H.; He, X.L.; Li, J.P.; Lin, C.L. Fabrication and ethanol sensing characteristics of ZnO nanowire gas sensors. *Appl. Phys. Lett.* **2004**, *84*, 3654–3656. [[CrossRef](#)]
52. Xu, H.; Liu, X.; Cui, D.; Li, M.; Jiang, M. A novel method for improving the performance of ZnO gas sensors. *Sens. Actuators B Chem.* **2006**, *114*, 301–307. [[CrossRef](#)]
53. Karunagaran, B.; Uthirakumar, P.; Chung, S.J.; Velumani, S.; Suh, E.-K. TiO₂ thin film gas sensor for monitoring ammonia. *Mater. Charact.* **2007**, *58*, 680–684. [[CrossRef](#)]
54. Gupta, S.K.; Joshi, A.; Kaur, M. Development of gas sensors using ZnO nanostructures. *J. Chem. Sci.* **2010**, *122*, 57–62. [[CrossRef](#)]
55. Zhang, T.; Nix, M.B.; Yoo, B.; Deshusses, M.A.; Myung, N.V. Electrochemically functionalized single-walled carbon nanotube gas sensor. *Electroanal. Int. J. Devoted Fundam. Pract. Asp. Electroanal.* **2006**, *18*, 1153–1158. [[CrossRef](#)]
56. Kumar, D.; Chaturvedi, P.; Saho, P.; Jha, P.; Chouksey, A.; Lal, M.; Rawat, J.; Tandon, R.P.; Chaudhury, P.K. Effect of single wall carbon nanotube networks on gas sensor response and detection limit. *Sens. Actuators B Chem.* **2017**, *240*, 1134–1140. [[CrossRef](#)]
57. Young, S.J.; Lin, Z.D. Ethanol gas sensors based on multi-wall carbon nanotubes on oxidized Si substrate. *Microsyst. Technol.* **2018**, *24*, 55–58. [[CrossRef](#)]
58. Young, S.-J.; Liu, Y.-H.; Lin, Z.-D.; Ahmed, K.; Shiblee, M.D.N.I.; Romanuik, S.; Sekhar, P.K.; Thundat, T.; Nagahara, L.; Arya, S. Multi-walled carbon nanotubes decorated with silver nanoparticles for acetone gas sensing at room temperature. *J. Electrochem. Soc.* **2020**, *167*, 167519. [[CrossRef](#)]
59. Yoon, H.J.; Yang, J.H.; Zhou, Z.; Yang, S.S.; Cheng, M.M.-C. Carbon dioxide gas sensor using a graphene sheet. *Sens. Actuators B Chem.* **2011**, *157*, 310–313. [[CrossRef](#)]
60. Chung, M.G.; Lee, H.M.; Kim, T.; Choi, J.H.; kyun Seo, D.; Yoo, J.-B.; Hong, S.-H.; Kang, T.J.; Kim, Y.H. Highly sensitive NO₂ gas sensor based on ozone treated graphene. *Sens. Actuators B Chem.* **2012**, *166*, 172–176. [[CrossRef](#)]

61. Lipatov, A.; Varezchnikov, A.; Wilson, P.; Sysoev, V.; Kolmakov, A.; Sinitkii, A. Highly selective gas sensor arrays based on thermally reduced graphene oxide. *Nanoscale* **2013**, *5*, 5426–5434. [[CrossRef](#)]
62. Yuan, W.; Shi, G. Graphene-based gas sensors. *J. Mater. Chem. A* **2013**, *1*, 10078–10091. [[CrossRef](#)]
63. Baek, D.-H.; Kim, J. MoS₂ gas sensor functionalized by Pd for the detection of hydrogen. *Sens. Actuators B Chem.* **2017**, *250*, 686–691. [[CrossRef](#)]
64. Kim, Y.; Kang, S.-K.; Oh, N.-C.; Lee, H.-D.; Lee, S.-M.; Park, J.; Kim, H. Improved sensitivity in Schottky contacted two-dimensional MoS₂ gas sensor. *ACS Appl. Mater. Interfaces* **2019**, *11*, 38902–38909. [[CrossRef](#)] [[PubMed](#)]
65. Pham, T.; Li, G.; Bekyarova, E.; Itkis, M.E.; Mulchandani, A. MoS₂-based optoelectronic gas sensor with sub-parts-per-billion limit of NO₂ gas detection. *ACS Nano* **2019**, *13*, 3196–3205. [[CrossRef](#)] [[PubMed](#)]
66. Suh, J.M.; Shim, Y.-S.; Kwon, K.C.; Jeon, J.-M.; Lee, T.H.; Shokouhimehr, M.; Jang, H.W. Pd-and Au-decorated MoS₂ gas sensors for enhanced selectivity. *Electron. Mater. Lett.* **2019**, *15*, 368–376. [[CrossRef](#)]
67. Imai, Y.; Kimura, Y.; Niwano, M. Organic hydrogen gas sensor with palladium-coated β -phase poly(vinylidene fluoride) thin films. *Appl. Phys. Lett.* **2012**, *101*, 181907. [[CrossRef](#)]
68. Cavallari, M.R.; Izquierdo, J.E.E.; Braga, G.S.; Dirani, E.A.T.; Pereira-da-Silva, M.A.; Rodríguez, E.F.G.; Fonseca, F.J. Enhanced sensitivity of gas sensor based on poly(3-hexylthiophene) thin-film transistors for disease diagnosis and environment monitoring. *Sensors* **2015**, *15*, 9592–9609. [[CrossRef](#)] [[PubMed](#)]
69. Han, S.; Zhuang, X.; Shi, W.; Yang, X.; Li, L.; Yu, J. Poly(3-hexylthiophene)/polystyrene (P3HT/PS) blends based organic field-effect transistor ammonia gas sensor. *Sens. Actuators B Chem.* **2016**, *225*, 10–15. [[CrossRef](#)]
70. Pasha, A.; Khasim, S.; Khan, F.A.; Dhananjaya, N. Fabrication of gas sensor device using poly(3,4-ethylenedioxythiophene)-poly(styrenesulfonate)-doped reduced graphene oxide organic thin films for detection of ammonia gas at room temperature. *Iran. Polym. J.* **2019**, *28*, 183–192. [[CrossRef](#)]
71. Martinelli, G.; Carotta, M.C.; Ferroni, M.; Sadaoka, Y.; Traversa, E. Screen-printed perovskite-type thick films as gas sensors for environmental monitoring. *Sens. Actuators B Chem.* **1999**, *55*, 99–110. [[CrossRef](#)]
72. Cerdà, J.; Arbiol, J.; Dezanneau, G.; Diaz, R.; Morante, J.R. Perovskite-type BaSnO₃ powders for high temperature gas sensor applications. *Sens. Actuators B Chem.* **2002**, *84*, 21–25. [[CrossRef](#)]
73. Zhuang, Y.; Yuan, W.; Qian, L.; Chen, S.; Shi, G. High-performance gas sensors based on a thiocyanate ion-doped organometal halide perovskite. *Phys. Chem. Chem. Phys.* **2017**, *19*, 12876–12881. [[CrossRef](#)]
74. Wang, J.; Ren, Y.; Liu, H.; Li, Z.; Liu, X.; Deng, Y.; Fang, X. Ultrathin 2D NbWO₆ Perovskite Semiconductor Based Gas Sensors with Ultrahigh Selectivity under Low Working Temperature. *Adv. Mater.* **2022**, *34*, 2104958. [[CrossRef](#)]
75. Zhao, C.; Fu, J.; Zhang, Z.; Xie, E. Enhanced ethanol sensing performance of porous ultrathin NiO nanosheets with neck-connected networks. *Rsc Adv.* **2013**, *3*, 4018–4023. [[CrossRef](#)]
76. Zeng, W.; Liu, Y.; Chen, G.; Zhan, H.; Mei, J.; Luo, N.; He, Z.; Tang, C. SnO–Sn₃O₄ heterostructural gas sensor with high response and selectivity to parts-per-billion-level NO₂ at low operating temperature. *RSC Adv.* **2020**, *10*, 29843–29854. [[CrossRef](#)]
77. Nakate, U.T.; Ahmad, R.; Patil, P.; Yu, Y.T.; Hahn, Y.-B. Ultra thin NiO nanosheets for high performance hydrogen gas sensor device. *Appl. Surf. Sci.* **2020**, *506*, 144971. [[CrossRef](#)]
78. Li, Y.; Chen, N.; Deng, D.; Xing, X.; Xiao, X.; Wang, Y. Formaldehyde detection: SnO₂ microspheres for formaldehyde gas sensor with high sensitivity, fast response/recovery and good selectivity. *Sens. Actuators B Chem.* **2017**, *238*, 264–273. [[CrossRef](#)]
79. Wu, Z.; Li, Z.; Li, H.; Sun, M.; Han, S.; Cai, C.; Shen, W.; Fu, Y. Ultrafast response/recovery and high selectivity of the H₂S gas sensor based on α -Fe₂O₃ nano-ellipsoids from one-step hydrothermal synthesis. *ACS Appl. Mater. Interfaces* **2019**, *11*, 12761–12769. [[CrossRef](#)]
80. Zhang, X.; Sun, J.; Tang, K.; Wang, H.; Chen, T.; Jiang, K.; Zhou, T.; Quan, H.; Guo, R. Ultralow detection limit and ultrafast response/recovery of the H₂ gas sensor based on Pd-doped rGO/ZnO-SnO₂ from hydrothermal synthesis. *Microsystems Nanoeng.* **2022**, *8*, 67. [[CrossRef](#)]
81. Lee, J.-H.; Kim, J.-H.; Kim, J.-Y.; Mirzaei, A.; Kim, H.W.; Kim, S.S. ppb-Level selective hydrogen gas detection of Pd-functionalized In₂O₃-loaded ZnO nanofiber gas sensors. *Sensors* **2019**, *19*, 4276. [[CrossRef](#)] [[PubMed](#)]
82. Lee, J.-H.; Kim, J.-Y.; Kim, J.-H.; Kim, S.S. Enhanced hydrogen detection in ppb-level by electrospun SnO₂-loaded ZnO nanofibers. *Sensors* **2019**, *19*, 726. [[CrossRef](#)] [[PubMed](#)]
83. Sui, N.; Zhang, P.; Zhou, T.; Zhang, T. Selective ppb-level ozone gas sensor based on hierarchical branch-like In₂O₃ nanostructure. *Sens. Actuators B Chem.* **2021**, *336*, 129612. [[CrossRef](#)]
84. Su, P.-G.; Zheng, Y.-L. Room-temperature ppb-level SO₂ gas sensors based on RGO/WO₃ and MWCNTs/WO₃ nanocomposites. *Anal. Methods* **2021**, *13*, 782–788. [[CrossRef](#)] [[PubMed](#)]
85. Murali, G.; Reddeppa, M.; Seshendra Reddy, C.; Park, S.; Chandrakalavathi, T.; Kim, M.-D.; In, I. Enhancing the charge carrier separation and transport via nitrogen-doped graphene quantum dot-TiO₂ nanoplate hybrid structure for an efficient NO gas sensor. *ACS Appl. Mater. Interfaces* **2020**, *12*, 13428–13436. [[CrossRef](#)] [[PubMed](#)]
86. He, H.; Guo, J.; Zhao, J.; Xu, J.; Zhao, C.; Gao, Z.; Song, Y.-Y. Engineering CuMOF in TiO₂ Nanochannels as Flexible Gas Sensor for High-Performance NO Detection at Room Temperature. *ACS Sens.* **2022**, *7*, 2750–2758. [[CrossRef](#)] [[PubMed](#)]
87. Wang, J.; Shen, Y.; Li, X.; Xia, Y.; Yang, C. Synergistic effects of UV activation and surface oxygen vacancies on the room-temperature NO₂ gas sensing performance of ZnO nanowires. *Sens. Actuators B Chem.* **2019**, *298*, 126858. [[CrossRef](#)]

88. Kumar, R.; Goel, N.; Kumar, M. UV-activated MoS₂ based fast and reversible NO₂ sensor at room temperature. *ACS Sens.* **2017**, *2*, 1744–1752. [[CrossRef](#)] [[PubMed](#)]
89. Drozdowska, K.; Rehman, A.; Krajewska, A.; Lioubtchenko, D.V.; Pavlov, K.; Rumyantsev, S.; Smulko, J.; Cywiński, G. Effects of UV light irradiation on fluctuation enhanced gas sensing by carbon nanotube networks. *Sens. Actuators B Chem.* **2022**, *352*, 131069. [[CrossRef](#)]
90. Li, Y.; Jin, H.; Sun, G.; Zhang, B.; Luo, N.; Lin, L.; Bala, H.; Cao, J.; Zhang, Z.; Wang, Y. Synthesis of novel porous ZnO octahedrons and their improved UV-light activated formaldehyde-sensing performance by Au decoration. *Phys. E Low-Dimens. Syst. Nanostruct.* **2019**, *106*, 40–44. [[CrossRef](#)]
91. Chang, H.-K.; Ko, D.-S.; Cho, D.-H.; Kim, S.; Lee, H.-N.; Lee, H.S.; Kim, H.-J.; Park, T.J.; Park, Y.M. Enhanced response of the photoactive gas sensor on formaldehyde using porous SnO₂@ TiO₂ heterostructure driven by gas-flow thermal evaporation and atomic layer deposition. *Ceram. Int.* **2021**, *47*, 5985–5992. [[CrossRef](#)]
92. Yang, Y.; Wu, S.; Cao, Y.; Li, S.; Xie, T.; Lin, Y.; Li, Z. A highly efficient room-temperature formaldehyde gas sensor based on a Ni-doped ZnO hierarchical porous structure decorated with NiS illuminated by UV light. *J. Alloys Compd.* **2022**, *920*, 165850. [[CrossRef](#)]
93. Seif, A.M.; Nikfarjam, A.; Hajghassem, H. UV enhanced ammonia gas sensing properties of PANI/TiO₂ core-shell nanofibers. *Sens. Actuators B Chem.* **2019**, *298*, 126906.
94. Zhou, Y.; Li, X.; Wang, Y.; Tai, H.; Guo, Y. UV Illumination-enhanced molecular ammonia detection based on a ternary-reduced graphene oxide–titanium dioxide–Au composite film at room temperature. *Anal. Chem.* **2018**, *91*, 3311–3318. [[CrossRef](#)] [[PubMed](#)]
95. Yang, Y.; Yu, S.; Guo, J.; Zhang, D. UV-enhanced highly sensitive ammonia sensing properties based on 2DPI/In₂O₃ heterostructure at room temperature. *J. Alloys Compd.* **2022**, *920*, 165878. [[CrossRef](#)]
96. Chinh, N.D.; Hien, T.T.; Do Van, L.; Hieu, N.M.; Quang, N.D.; Lee, S.-M.; Kim, C.; Kim, D. Adsorption/desorption kinetics of nitric oxide on zinc oxide nano film sensor enhanced by light irradiation and gold-nanoparticles decoration. *Sens. Actuators B Chem.* **2019**, *281*, 262–272. [[CrossRef](#)]
97. Xie, Y.; Yu, S.; Zhong, Y.; Zhang, Q.; Zhou, Y. SnO₂/graphene quantum dots composited photocatalyst for efficient nitric oxide oxidation under visible light. *Appl. Surf. Sci.* **2018**, *448*, 655–661. [[CrossRef](#)]
98. Geng, Y.; Chen, D.; Li, N.; Xu, Q.; Li, H.; He, J.; Lu, J. Z-Scheme 2D/2D α -Fe₂O₃/g-C₃N₄ heterojunction for photocatalytic oxidation of nitric oxide. *Appl. Catal. B Environ.* **2021**, *280*, 119409. [[CrossRef](#)]
99. Zhang, B.; Bao, N.; Wang, T.; Xu, Y.; Dong, Y.; Ni, Y.; Yu, P.; Wei, Q.; Wang, J.; Guo, L. High-performance room temperature NO₂ gas sensor based on visible light irradiated In₂O₃ nanowires. *J. Alloys Compd.* **2021**, *867*, 159076. [[CrossRef](#)]
100. Chen, P.; Hu, J.; Yin, M.; Bai, W.; Chen, X.; Zhang, Y. MoS₂ nanoflowers decorated with Au nanoparticles for visible-light-enhanced gas sensing. *ACS Appl. Nano Mater.* **2021**, *4*, 5981–5991. [[CrossRef](#)]
101. Geng, X.; Lu, P.; Zhang, C.; Lahem, D.; Olivier, M.-G.; Debliquy, M. Room-temperature NO₂ gas sensors based on rGO@ ZnO_{1-x} composites: Experiments and molecular dynamics simulation. *Sens. Actuators B Chem.* **2019**, *282*, 690–702. [[CrossRef](#)]
102. Song, Y.; Zhang, Y.; Ma, M.; Ren, J.; Liu, C.; Tan, J. Visible light-assisted formaldehyde sensor based on HoFeO₃ nanoparticles with sub-ppm detection limit. *Ceram. Int.* **2020**, *46*, 16337–16344. [[CrossRef](#)]
103. Wang, J.; Deng, H.; Li, X.; Yang, C.; Xia, Y. Visible-light photocatalysis enhanced room-temperature formaldehyde gas sensing by MoS₂/rGO hybrids. *Sens. Actuators B Chem.* **2020**, *304*, 127317. [[CrossRef](#)]
104. Huang, J.; Jiang, D.; Zhou, J.; Ye, J.; Sun, Y.; Li, X.; Geng, Y.; Wang, J.; Du, Y.; Qian, Z. Visible light-activated room temperature NH₃ sensor base on CuPc-loaded ZnO nanorods. *Sens. Actuators B Chem.* **2021**, *327*, 128911. [[CrossRef](#)]
105. Shao, X.; Wang, S.; Hu, L.; Liu, T.; Wang, X.; Yin, G.; Zhou, T.; Rajan, R.; Jia, F.; Liu, B. Improvement of Gas Sensing of Uniform Ag₃PO₄ Nanoparticles to NH₃ under the Assistant of LED Lamp with Low Power Consumption at Room Temperature. *ChemistrySelect* **2021**, *6*, 8338–8344. [[CrossRef](#)]
106. Lin, Y.-T.; Yu, S.-Y.; Zan, H.-W.; Yeh, P.-H.; Lu, C.-J.; Meng, H.-F.; Luo, C.-W.; Soppera, O. Photo-assisted recovery in ammonia sensor based on organic vertical diode. *Org. Electron.* **2019**, *67*, 272–278. [[CrossRef](#)]